

Magmatic-dominated fluid evolution in the Jurassic Nambija gold skarn deposits (southeastern Ecuador)

Jean Vallance · Lluís Fontboté · Massimo Chiaradia ·
Agnès Markowski · Susanne Schmidt ·
Torsten Vennemann

Received: 3 January 2009 / Accepted: 11 March 2009 / Published online: 31 March 2009
© Springer-Verlag 2009

Abstract The Jurassic (approximately 145 Ma) Nambija oxidized gold skarns are hosted by the Triassic volcanosedimentary Piuntza unit in the sub-Andean zone of southeastern Ecuador. The skarns consist dominantly of granditic garnet (Ad_{20-98}) with subordinate pyroxene ($\text{Di}_{46-92}\text{Hd}_{17-42}\text{Jo}_{0-19}$) and epidote and are spatially associated with porphyritic quartz-diorite to granodiorite intrusions. Endoskarn is developed at the intrusion margins and grades inwards into a potassic alteration zone. Exoskarn has an outer K- and Na-enriched zone in the volcanosedimentary unit. Gold mineralization is associated with the weakly developed retrograde alteration of the exoskarn and occurs mainly in sulfide-poor vugs and milky quartz veins and veinlets in association with hematite. Fluid inclusion data for the main

part of the prograde stage indicate the coexistence of high-temperature (500°C to >600°C), high-salinity (up to 65 wt.% eq. NaCl), and moderate- to low-salinity aqueous-carbonic fluids interpreted to have been trapped at pressures around 100–120 MPa, corresponding to about 4-km depth. Lower-temperature (510–300°C) and moderate- to low-salinity (23–2 wt.% eq. NaCl) aqueous fluids are recorded in garnet and epidote of the end of the prograde stage. The microthermometric data (Th from 513°C to 318°C and salinity from 1.0 to 23 wt.% eq. NaCl) and $\delta^{18}\text{O}$ values between 6.2‰ and 11.5‰ for gold-bearing milky quartz from the retrograde stage suggest that the ore-forming fluid was dominantly magmatic. Pressures during the early retrograde stage were in the range of 50–100 MPa, in line with the evidence for CO_2 effervescence and probable local boiling. The dominance of magmatic low-saline to moderately saline oxidizing fluids during the retrograde stage is consistent with the depth of the skarn system, which could have delayed the ingress of external fluids until relatively low temperatures were reached. The resulting low water-to-rock ratios explain the weak retrograde alteration and the compositional variability of chlorite, essentially controlled by host rock compositions. Gold was precipitated at this stage as a result of cooling and pH increase related to CO_2 effervescence, which both result in destabilization of gold-bearing chloride complexes. Significant ingress of external fluids took place after gold deposition only, as recorded by $\delta^{18}\text{O}$ values of 0.4‰ to 6.2‰ for fluids depositing quartz (below 350°C) in sulfide-rich barren veins. Low-temperature (<300°C) meteoric fluids ($\delta^{18}\text{O}_{\text{water}}$ between -10.0‰ and -2.0‰) are responsible for the precipitation of late comb quartz and calcite in cavities and veins and indicate mixing with cooler fluids of higher salinities (about 100°C and 25 wt.% eq. NaCl). The latter are similar to low-temperature fluids (202–74.5°C)

Editorial handling: B. Lehmann

J. Vallance (✉) · L. Fontboté · M. Chiaradia · S. Schmidt
Section des Sciences de la Terre et de l'Environnement,
Université de Genève,
Rue des Maraîchers 13, 1205,
Geneva, Switzerland
e-mail: jvallance@passac.com.pe

J. Vallance
Pan American Silver Peru SAC,
Av. La Floresta 497, Of. 301, Chacarilla del Estanque, San Borja,
Lima, Peru

A. Markowski
Isotopengeologie und Mineralische Rohstoffe, ETH-Zentrum,
C61.1, Sonneggstrasse 5, 8092,
Zurich, Switzerland

T. Vennemann
Institut de Minéralogie et Géochimie, Université de Lausanne,
L'Anthropôle,
1015 Lausanne, Switzerland

with $\delta^{18}\text{O}$ values of -0.5‰ to 3.1‰ and salinities in the range of 21.1 to 17.3 wt.% eq. CaCl_2 , trapped in calcite of late veins and interpreted as basinal brines. Nambija represents a deep equivalent of the oxidized gold skarn class, the presence of CO_2 in the fluids being partly a consequence of the relatively deep setting at about 4-km depth. As in other Au-bearing skarn deposits, not only the prograde stage but also the gold-precipitating retrograde stage is dominated by fluids of magmatic origin.

Keywords Gold · Skarn · Aqueous-carbonic fluids · Oxygen isotope · Chlorite · Nambija · Ecuador

Introduction

Skarns are an important source of gold either as the main commodity or as a by-product. Skarns from which gold is extracted as the unique or main commodity are known as gold skarns (e.g., Meinert 2000) and have been subdivided into reduced, oxidized, magnesian, and metamorphic types according to the mineralogy of the dominant silicate phase (characterized either by Fe^{2+} , Fe^{3+} , or Mg^{2+}) or the geological context (e.g., metamorphism-related for metamorphic gold skarns). The majority of gold production from skarns is derived from oxidized skarns in which gold is mined as a by-product of copper. Most of these skarns contain <1 g/t Au, although in Cu-rich ores Au can reach higher grades (Meinert 2000). Few detailed fluid inclusion studies on the fluid evolution in oxidized gold skarn deposits are, however, available in the literature (e.g., Mc Coy and Wabu gold skarns, Brooks et al. 1991; Brooks 1994; Allen and Aslund 1998).

The Nambija oxidized gold skarn district is one of the main gold producers of Ecuador (see Chiaradia et al. 2009) and is economically and scientifically interesting because of a high average gold grade of 15 g/t Au, with some ore zones having grades as high as 300 g/t Au. These features set Nambija apart from most oxidized gold skarns and have prompted this detailed study of the physicochemical evolution of the ore fluids in the skarns.

Nambija is located in the sub-Andean zone of southeastern Ecuador, 40 km west of the Peruvian border (Fig. 1). The district includes several mines detailed in Fig. 1 and in the companion paper of Chiaradia et al. (2009).

The results of previous studies on the Nambija district (Vallance et al. 2003; Fontboté et al. 2004; Markowski et al. 2006; Chiaradia et al. 2009) have shown that the prograde-stage skarn, consisting dominantly of granditic garnet with subordinate pyroxene and epidote, is of the oxidized type and is associated in time and space with granodioritic and quartz-dioritic porphyritic intrusions of the Jurassic Panguí porphyry belt (Gendall et al. 2000; Chiaradia et al. 2009).

No mineralogical zonation has been observed at the mine scale, except at Fortuna. The main ore mineral associated with gold is hematite indicating oxidizing conditions at the time of gold deposition. U–Pb age determinations of magmatic zircon and endoskarn titanite from porphyritic intrusions at Fortuna and Campanillas as well as Re–Os ages of post-gold molybdenite is indistinguishable and constrain gold deposition at approximately 145 Ma (Chiaradia et al. 2009). This suggests that the Nambija district is part of the same metallogenic event responsible for the Late Jurassic El Panguí porphyry Cu belt in the sub-Andean zone of southeastern Ecuador (Gendall et al. 2000; Chiaradia et al. 2009). The results point to a direct relationship between skarnification and gold ore as previously suggested by Hammarstrom (1992).

The present contribution refines certain aspects of the description of skarn and K and Na metasomatism affecting both the porphyritic intrusions and the volcanoclastic host rocks. The main focus is placed on the nature and evolution of the hydrothermal fluid in the Nambija oxidized gold skarn deposits. This is obtained through newly acquired microthermometric and Raman data, as well as stable isotope analyses of quartz and calcite. The study integrates previous fluid inclusion data of Fontboté et al. (2004) and Markowski et al. (2006). The data suggest that both the prograde skarn and the weakly developed retrograde alteration were dominated by magmatic fluids and that the mineralization process at Nambija took place at deeper levels than other oxidized gold skarns.

Geological setting

The regional geology and geochronology of the Nambija district is summarized in the companion paper (Chiaradia et al. 2009) and in previous work (Vallance et al. 2003; Fontboté et al. 2004; Markowski et al. 2006). Briefly, the skarn bodies are hosted by the Triassic volcanosedimentary Piuntza unit, which occurs as a roof pendant within the Jurassic-I-type granodioritic to tonalitic Zamora Batholith. The Piuntza unit and the Zamora Batholith are cut by several felsic porphyritic intrusions (quartz-diorite to granodiorite at the Fortuna, Cambana, and Campanillas deposits, Fig. 1), which form outcrops of several tens to hundreds of meters in length, as well as by dikes up to 5–7 m thick. Some of these intrusions, like Cumay, 2 km north of the Fortuna mine (Fig. 1), are mineralized with copper and molybdenum or with copper and gold (Prodeminca 2000), and all are overprinted by extensive K–Na metasomatism. Plagioclase is the most abundant phenocryst phase together with K-feldspar in a quartzo-feldspathic groundmass. Biotite is rare, and green hornblende is the main mafic mineral. Two of these porphyritic intrusions have been

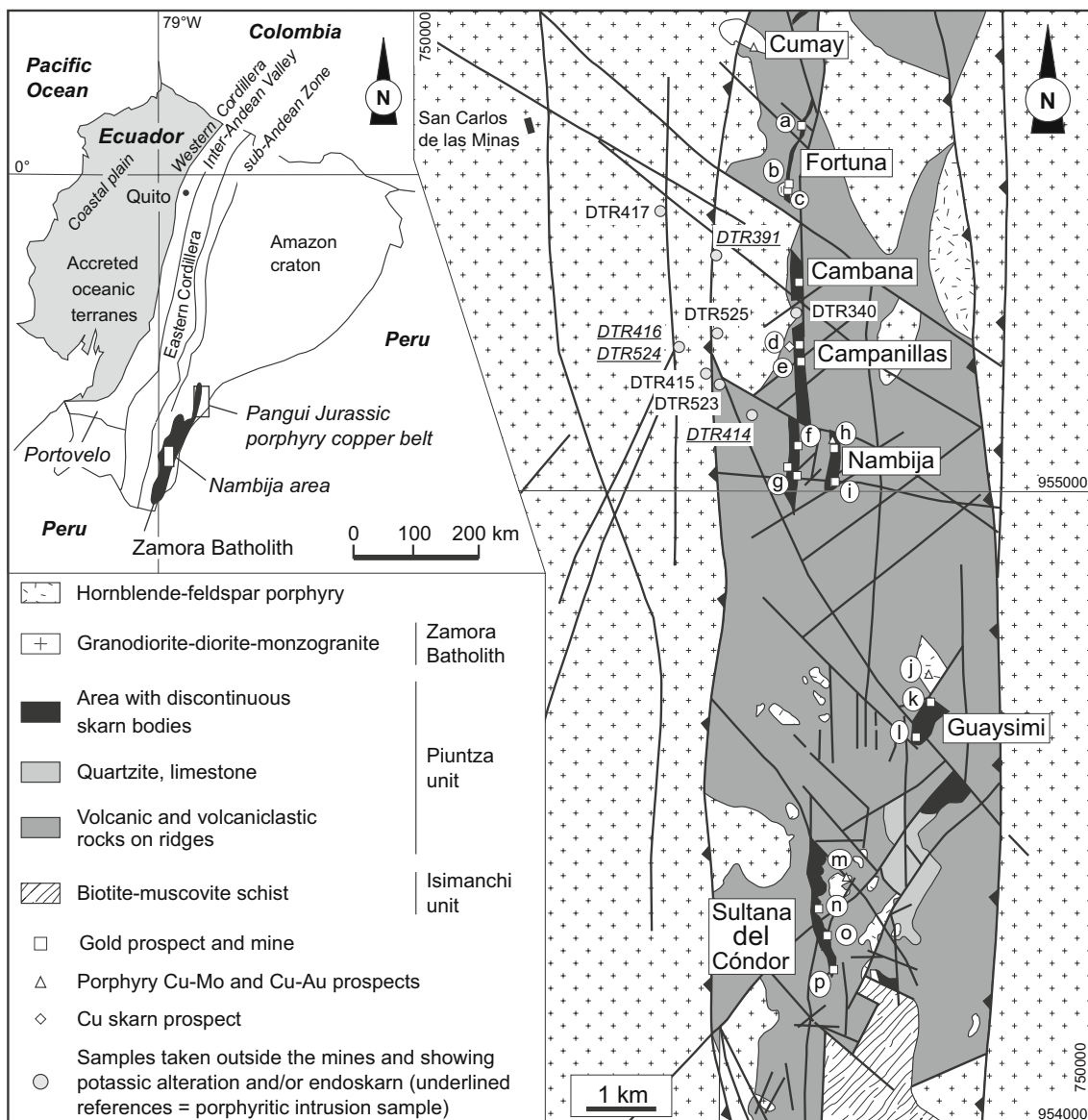


Fig. 1 Structural map of Ecuador (modified from Litherland et al. 1994; Pratt et al. 2005) showing the location of the Nambija district and the Zamora Batholith and simplified geologic map of the Nambija district (modified from Prodemínca 2000) with location of the samples taken outside the mines. *a* Cumay Cu–Mo porphyry (prospect), *b* Fortuna Cuerpo 3 (prospect), *c* Fortuna Mine 1 (abandoned workings), *d* Fortuna Mine 2 and Southern Sector (open pit), *e* Cambana (open pit), *f* Campanillas-Katy (abandoned workings), *g* Campanillas main present workings (open pit and underground), *h* Nambija-El Arco

(open pit and underground), *i* Nambija-El Playón-Mapasingue (underground), *j* Nambija-El Tierrero gold skarn and Cu–Mo porphyry (open pit and underground), *k* Nambija-El Diamante (prospect), *l* David Cu–Mo porphyry (prospect), *m* Guaysimi-Banderas (open pit), *n* Guaysimi central (open pit), *o* Cerro Colorado-Tumi Cu–Au porphyry (prospect), *p* Sultana del Cóndor-Bruce (open pit and underground), *q* Sultana del Cóndor central (open pit and underground), *r* Sultana del Cóndor-Toscón (open pit and underground)

dated at 145.38 ± 0.14 Ma (U–Pb on zircon, Chiaradia et al. 2009).

Four main sets of structures are found in the Nambija district (Fig. 1). The first is represented by a conjugate system of N–S dextral reverse faults (which limit the district to the east and to the west) and NE-trending steeply dipping faults with locally sinistral displacement and/or tensional character. The main gold mineralization and most retrograde

alteration minerals studied in the present work are controlled by these NE-striking faults. A second set, identified in the Guaysimi mine (Fig. 1), consists of ENE–WSW- to E–W-trending steeply dipping normal faults in part sealed by calcite. The third set cuts the previous structures and consists of NW-striking reverse faults and thrust planes dipping 10–40° to SW. A fourth set of E-striking steeply dipping normal dextral faults crosscuts all previous structures.

Analytical methods

Microthermometric analyses were made on 70- to 100- μm -thick doubly polished rock sections. A Linkam THMSG600 heating and freezing stage mounted on a DMLB Leica microscope equipped with a Nikon $\times 100$ long-working-distance lens was used for the microthermometric measurements, as described by Shepherd (1981). The system was calibrated with synthetic fluid inclusions at -56.6°C , 0.0°C , and 374.1°C (Sterner and Bodnar 1984). Low-temperature measurements have an uncertainty of $\pm 0.1^\circ\text{C}$, whereas high-temperature measurements have a precision of $\pm 1^\circ\text{C}$. Salinities were calculated in the $\text{NaCl-H}_2\text{O}$ system from final ice melting temperatures between 0.0°C and -21.1°C , using equations published in Bodnar and Vityk (1994) and in the $\text{CaCl}_2\text{-H}_2\text{O}$ system for ice melting temperatures below -21.1°C with a eutectic around -52°C , using the equation of Oakes et al. (1990). Salinities of halite-bearing (\pm sylvite-bearing) inclusions were calculated using the equation of Sterner et al. (1988) and the computer program AqSol1e of Bakker and Brown (2003). Bulk compositions and isochores of aqueous-carbonic fluid inclusions were modeled with the ICE, Q2, NOSALT, BULK, and ISOC computer programs of Bakker and Brown (2003).

Raman measurements were conducted using a Jobin-Yvon Labram Raman microprobe with a modified Olympus microscope. Raman spectra were recorded using an incident laser wavelength of 532 nm from a Coherent DPSS 534 neodymium-doped yttrium aluminum garnet laser following the procedures of Dubessy et al. (1989) and Burke (2001).

Chlorites were analyzed at the Institute of Mineralogy and Geochemistry of Lausanne (Switzerland) on a Cameca Camebax SX 50 electron microprobe using a 15-nA beam current and a 15-kV acceleration voltage.

Oxygen isotope analyses were made at the Institute of Mineralogy and Geochemistry of Lausanne in Switzerland. The oxygen isotope composition (^{16}O , ^{18}O) of the quartz samples were measured using a method similar to that described by Sharp (1990) and Rumble and Hoering (1994) and that is described in more detail in Kasemann et al. (2001). Between 0.5 and 2 mg of sample was loaded onto a small Pt sample holder and pumped out to a vacuum of about 10^{-6} mbar. After prefluorination of the sample chamber overnight, the samples were heated with a CO_2 laser in 50 mbar of pure F_2 . Excess F_2 was separated from the O_2 produced by conversion to Cl_2 using KCl held at 150°C . The extracted O_2 was collected on a molecular sieve ($13\times$) and subsequently expanded into the inlet of a Finnigan MAT 253 isotope ratio mass spectrometer. Oxygen isotope compositions are given in the standard δ notation, expressed relative to the Vienna Standard Mean Ocean Water in per mill (‰). Replicate oxygen isotope analyses of the standard used (Ls-1 Qtz, $n=6$) had an average precision of $\pm 0.08\text{‰}$

(one sigma) for $\delta^{18}\text{O}$. The accuracy of $\delta^{18}\text{O}$ values is commonly better than 0.2‰ compared to accepted $\delta^{18}\text{O}$ values for NBS-28 of 9.64‰ and UWG-2 of 5.8‰ (Valley et al. 1995). The C- and O- isotope composition of the carbonates was measured with a GasBench II connected to a Finnigan MAT DeltaPlus XL mass spectrometer, using a He-carrier gas system according to a method adapted after Spoetl and Vennemann (2003). Sample values were normalized using an in-house standard calibrated against $\delta^{13}\text{C}$ and $\delta^{18}\text{O}$ values of NBS-19 ($+1.95\text{‰}$ and -2.20‰ , relative to Vienna PeeDee Belemnite (VPDB)). External reproducibility for the analyses estimated from replicate analyses of the in-house standard ($n=6$) is $\pm 0.07\text{‰}$ for $\delta^{13}\text{C}$ and 0.08‰ for $\delta^{18}\text{O}$.

Skarns and gold quartz veins in the Nambija district

Exoskarn and endoskarn have replaced the Piuntza unit lithologies and the outer parts of the porphyritic intrusions, respectively. The endoskarn shows a gradual transition to an inner potassic alteration zone within the porphyritic intrusions, whereas the garnet-pyroxene exoskarn grades into an outer zone of K and Na metasomatism affecting the Piuntza unit volcanosedimentary rocks.

Endoskarn in porphyritic intrusion and inner potassic alteration

An *endoskarn* consisting of K-feldspar, actinolite, diopside, Na-rich plagioclase, titanite, quartz, apatite, and pyrite occurs at the margins of the porphyritic quartz-diorite intrusion at Fortuna (Markowski et al. 2006). Na-rich plagioclase and potassium feldspar have replaced the groundmass (up to 5.3 wt.% Na_2O and 3.6 wt.% K_2O) and the cores of the Ca-rich plagioclase phenocrysts. Hornblende has generally not been replaced except very locally where it is replaced by actinolite and very minor diopside. The best-studied example with inner *potassic alteration* occurs at Fortuna, where the main alteration assemblage consists of K-feldspar + titanite and subordinate biotite + magnetite. K_2O concentrations can be as high as 4.8 wt.%. Potassic feldspar typically has replaced most of the groundmass and forms overgrowths on the plagioclase phenocrysts, occasionally completely replacing it. Hornblende is mostly unaltered, only locally having been replaced by K-feldspar + titanite and subordinately by biotite + magnetite and/or titanite.

Quartz \pm K-feldspar veins up to 1 cm thick occur in the porphyritic quartz-diorite intrusion at Fortuna (Fig. 3) and have a low sulfide (pyrite only) content ($<1\%$). These veins show similar features to the “B veins” of porphyry systems (nomenclature of Gustafson and Hunt 1975) but are more continuous because they can be followed for several meters along an average NE–SW orientation with steep dips. The

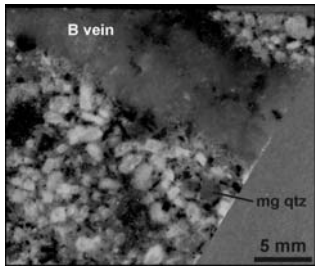
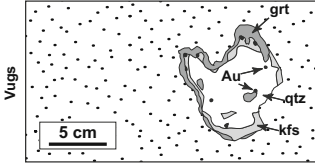
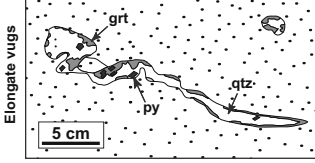
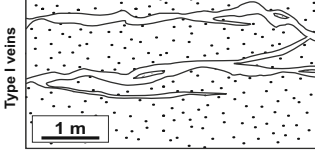
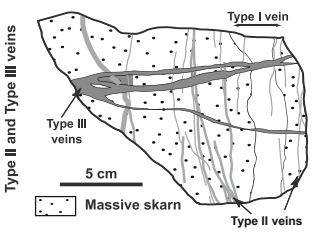
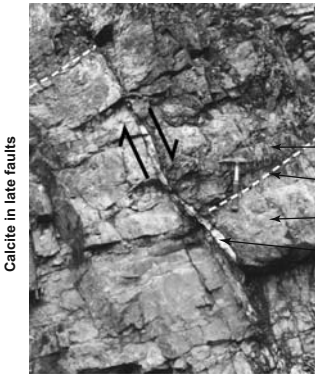
VUGS, VEINS AND THEIR FLUID INCLUSION CONTENT		
	Description	Fluid inclusion content
	<p>Magmatic quartz (mg qtz): rounded quartz phenocrysts up to 7 mm</p> <p>B veins: veins of quartz ± K-feldspar up to 1 cm thick in the quartz-diorite porphyritic intrusion at Fortuna. Low sulfide content exclusively constituted by pyrite (<1%).</p> <p>The veins lack alteration haloes and have a symmetrical structure with discontinuous K-feldspar bands at the walls, an intermediate zone of fine-grained K-feldspar + quartz, and a core of coarser quartz and minor amounts of pyrite</p> <p>Length up to a few meters with a general NE-SW orientation with steep dips.</p>	<p>Lh, Lc, L1, L2, and L3 (all secondary)</p> <p>Lh (primary), Lc (primary and secondary), L1 (primary and secondary), L2 (secondary), and L3 (secondary)</p>
	<p>Vugs and type I veins (N10-60°E) show irregular and discontinuous morphology with gradational contacts to massive skarn (the infilling minerals typically cement euhedral garnet at the vug/vein wall)</p> <p>Filling: mainly quartz, K-feldspar, calcite, chlorite, epidote ± plagioclase ± muscovite. Ore minerals < 2% (pyrite, hematite, sphalerite, chalcocopyrite, and native gold).</p>	<p>Lc (primary), L1 (primary), L2 (primary and secondary), L3 (secondary), and L3h (secondary)</p>
	<p>Width ranges from 1 mm to 15 cm, length up to a few meters (continuous transition to type I veins).</p> <p>They develop in places in volcanoclastic rocks but always within tens of centimeters of the skarn bodies.</p> <p>Best developed at Cambana, Campanillas, and Guaysimi.</p> <p>See also Fig. 2a</p>	<p>Lc (primary), L1 (primary), L2 (primary and secondary), L3 (secondary), and L3h (secondary)</p>
	<p>Widths range from 2 to 30 cm. Walls are better defined than in vugs particularly where cutting volcanoclastic rocks. Quartz-K-feldspar ratio is always >1:1.</p> <p>Highest gold grades.</p> <p>Typically well developed at Campanillas and to a lesser extent at Guaysimi and at Nambija, recognized at Cambana, but virtually absent at Fortuna.</p> <p>See also Fig. 2c</p>	<p>Lc (primary), L1 (primary), L2 (primary and secondary), L3 (secondary), and L3h (secondary)</p>
	<p>Throughgoing veins. Filling: similar mineralogy to type I veins but carbonates always present and sulfides more (II) to much more (III) abundant.</p> <p>Type II veins (N10-60°E) They are thin (<1 mm) and occur mostly as bundles of parallel veins. Sulfide content <5%.</p> <p>Typically well developed in the Guaysimi Central mine. Occur sometimes at Campanillas and in El Tierrero mine. Always cut type I veins See also Figs. 2c</p> <p>Type III veins (N70-100°E) Thickness is mainly in the range of 1 to 2 mm but up to a few cm. Sulfide content 5 to 50% (sphalerite and molybdenite observed). Well developed in the Katy area at Campanillas, in El Tierrero mine at Nambija, and at Guaysimi. Actinolite observed at Guaysimi Central See also Figs. 2c</p>	<p>L3 (primary, not studiable because of small size)</p> <p>L3 (primary, not studiable because of small size)</p>
<p>cf. Fig. 2E</p>	<p>Clear colorless to purple comb quartz ±chlorite ±calcite ±hematite filling cavities and veins.</p> <p>Thickness is mainly in the range of 0.5 to 1 cm but up to 7-8 cm cavities were observed at Campanillas</p>	<p>L3 (primary) and L3h (secondary)</p>
	<p>White calcite sealing ENE-WSW to E-W normal steeply dipping faults.</p> <p>Locally calcite cement brecciated skarn</p>	<p>L3 (primary)</p>

Fig. 2 Main features of retrograde vugs and veins (modified from Fontboté et al. 2004). Fluid inclusion types hosted in the infilling minerals are also indicated

veins lack alteration haloes and have a symmetrical structure with discontinuous K-feldspar bands at the walls, an intermediate zone of fine-grained K-feldspar + quartz, and a core of coarser quartz and minor amounts of pyrite.

At Campanillas, the endoskarn (although not completely obliterating the original rock texture) is more developed, with hornblende replaced by diopside and titanite (euhedral and twinned grains up to 7 mm in size) and diopside that has, in turn, been replaced by actinolite.

Garnet-pyroxene exoskarn and outer potassic-sodic alteration

The exoskarn occurs as massive, coarse-grained, and usually concordant bands that replaces mainly fine-grained volcanoclastic rocks (Fig. 2a). Less reactive or less permeable rock units such as quartzite, shale, and black shale are generally not skarnified. Carbonate rocks have only been recognized in drill core at the Nambija-El Diamante prospect and as a 30-cm-long and 5-cm-thick lens in massive garnet skarn at Guaysimi. At Fortuna, Markowski et al. (2006) recognized rare bioclasts.

The following main exoskarn types occur in the Nambija district (modified from Fontboté et al. 2004 and Markowski et al. 2006). An almost monomineralic *massive brown garnet skarn* (Ad_{20–98}) forms the main part of the calc-silicate bodies. A *green pyroxene* (Di_{46–92}Hd_{17–42}Jo_{0–19})-*epidote skarn* has developed at the margin of the brown garnet skarn at the outcrop scale and at the deposit scale at Fortuna. Patches of *blue–green skarn* occur within the brown garnet skarn as transitions to areas affected by retrograde alteration (Fig. 2a). The blue–green garnet skarn consists of dominantly euhedral granditic garnet (Ad_{9–99}), with minor amounts of pyroxene and epidote, in a matrix of anhedral milky quartz with occasional K-feldspar (Fig. 2b, d). All skarn types and volcanoclastic rocks are crosscut by honey-yellow andraditic garnet bands (Ad_{29–100}), which occur also as clusters.

A halo of K and Na metasomatism affects the volcanoclastic rocks of the Piuntza unit at the outer margin of the exoskarn (Markowski et al. 2006). Mineral associations related to K and Na metasomatism include Na-rich plagioclase, K-feldspar, pyroxene, actinolite with minor epidote, titanite, and rare garnet. Approaching the skarn, the original volcanoclastic texture is progressively obliterated, with 0.5- to 2-cm-thick discontinuous K-feldspar-albite/oligoclase rims against the pyroxene-epidote skarn and more exceptionally against the brown garnet skarn.

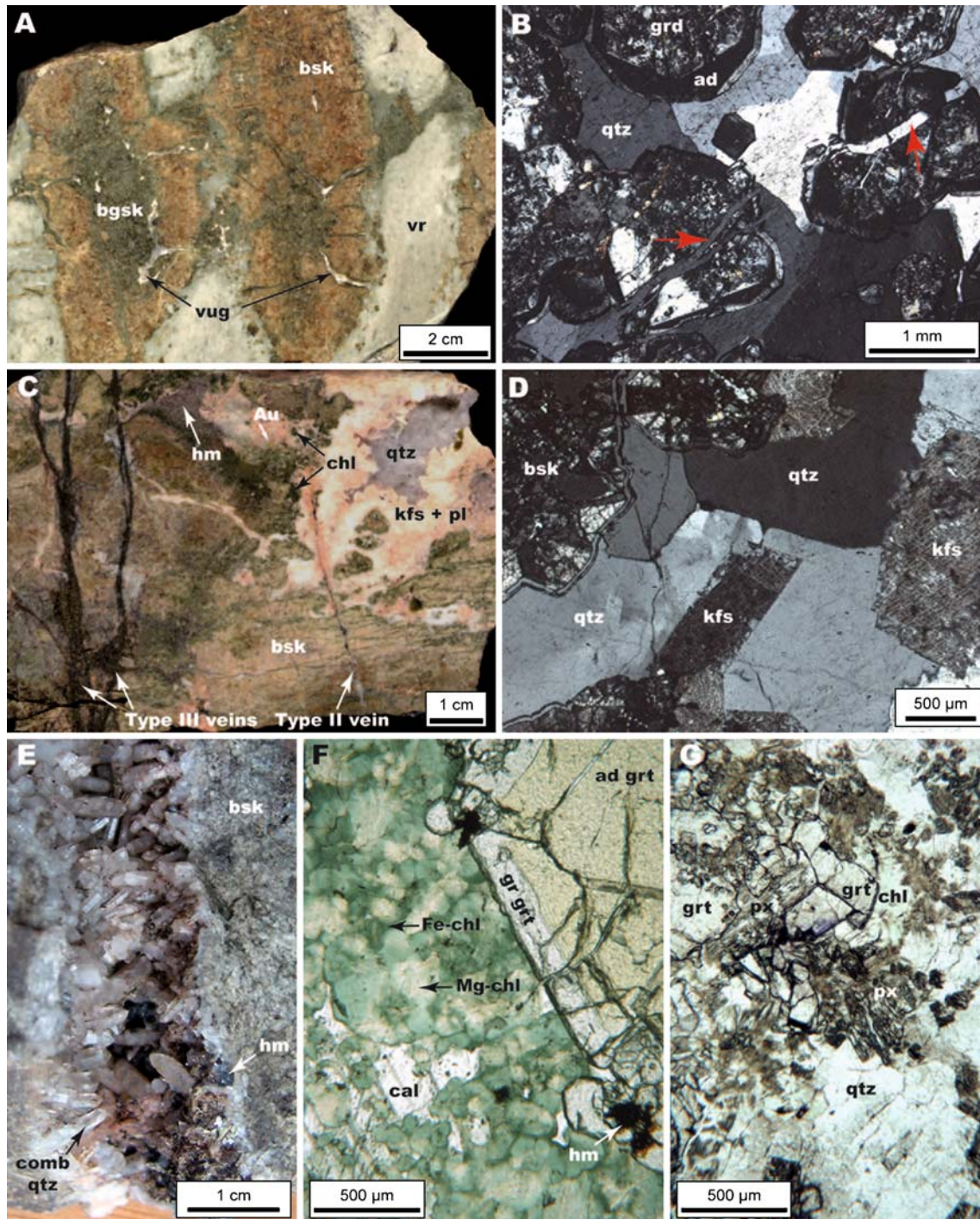
Retrograde stage and gold quartz veins

Gold mineralization is associated with the retrograde stage of the skarn, which is weakly developed and does not obliterate the prograde stage textures. Minerals of the retrograde stage are quartz, K-feldspar, calcite, chlorite, and

Fig. 3 Selected samples from the Nambija district showing typical skarn, vein, and retrograde mineral fabrics. **a** Massive brown garnet skarn (*bsk*) in fine-grained Na-metasomatized volcanoclastic rocks (*vr*). Patches of blue–green garnet skarn (*bgsk*) occur within the brown garnet skarn and show transition to vugs and elongated vugs mainly filled with milky quartz (core) and K-feldspar (walls). Sample DTR361, Guaysimi central pit. **b** Photomicrograph of blue–green garnet skarn. Euhedral anisotropic granditic garnet (*grd*) with isotropic late honey-yellow andraditic garnet overgrowth (*ad*) occurs in a matrix of milky quartz (*qtz*). The red arrows show a vein (type II) filled with quartz showing the same crystallographic orientation as host milky quartz. Sample DTR380, Campanillas mine (transmitted light, crossed polars). **c** Photograph of typical irregular high-grade type I vein in brown garnet skarn (*bsk*) in Guaysimi central pit. The vein is cut parallel to strike. It is mainly filled with K-feldspar (*kfs*) and Na-rich plagioclase (*pl*) at the walls and milky quartz (*qtz*) in the core. Other retrograde minerals are chlorite (*chl*) and hematite (*hm*). Gold (Au) builds grains up to several millimeters in size. The type I vein is cut by a thin type II vein and by late sulfide-rich type III veins. Sample DTR365. **d** Photomicrograph of milky quartz and K-feldspar filling a vug within the brown garnet skarn. Sample DTR334, Cambana mine (transmitted light, crossed polar). **e** Photograph of comb quartz (*comb qtz*) and hematite filling cavities within the brown garnet skarn. Sample DTR37, Campanillas mine. **f** Photomicrograph of calcite and zoned chlorite with yellowish Mg-rich core (*Mg-chl*) and dark green Fe-rich rims (*Fe-chl*), at the contact with late honey-yellow garnet in a type I vein. The garnet grain is zoned from andraditic core (*ad grt*) to granditic rim (*gr grt*). Sample DTR327, Campanillas mine (transmitted light, parallel polars). **g** Photomicrograph showing Mg-rich pale chlorite replacing preferentially diopside pyroxene (*px*) in pyroxene-rich blue–green garnet skarn. Sample DTR309, Cambana mine (transmitted light, parallel polars)

hematite, ±plagioclase, ±muscovite, plus minor amounts of epidote, pyrite, chalcopyrite, hematite, sphalerite, and gold. The retrograde overprint occurs mainly as mineral infillings in structurally controlled (N 010°–060° E) elongated vugs and up to several-centimeters-wide quartz-bearing veins of type I, type II, and type III (Figs. 2a, c, d and 3). Anhedral milky quartz, similar to that forming the matrix of the blue–green garnet skarn, constitutes most of the filling of vugs and type I veins (Fig. 2a, c, d and 3). Garnet occurs locally on the vug walls and in type I veins, suggesting a continuous transition from blue–green garnet skarn to type I veins. Gold deposition occurred preferentially in vugs and types I and II veins where hematite is the only opaque mineral in addition to native gold (Fig. 2c). Later sulfide-rich type III veins, which contain more than 50% of total sulfides (mainly pyrite) of the deposits, do not contain gold (Figs. 2c and 3). A late barren assemblage of clear colorless to purple comb quartz, ±chlorite, ±calcite, and ±hematite filling cavities and veins has been identified mainly in Campanillas (Fig. 2e).

The late retrograde stage is also recognized in the porphyritic intrusions, both in the endoskarn and the inner potassic zone. It is characterized by the formation of chlorite + epidote at the expense of diopside and early actinolite and of sericite + quartz at the expense of K-feldspar. Small amounts of euhedral pyrite and subordinate



chalcopyrite as disseminations and in through-going veins (type III veins, Fig. 3) are ascribed to this alteration stage.

Fluid inclusions: previous studies

Shepherd (1988 in Litherland et al.1994, 2000 in Prodeminca 2000; personal communication 2003) carried out the first fluid inclusion study on the Nambija mineral-

ization. He measured two-phase fluid inclusions in quartz from gold-bearing veins obtaining minimum trapping temperatures of between 220°C and 150°C and salinities ranging from 2 to 12 wt.% eq. NaCl with the mode at 2–4 wt.% eq. NaCl. Calcite occurring in the same veins displayed lower homogenization temperatures (140–130°C) and higher salinities (15–24 wt.% eq. NaCl). Laser ablation inductively coupled plasma mass spectrometry bulk analyses of the low-salinity fluid inclusions

from molybdenite-bearing quartz veins (our type III veins) of El Tierrero mine indicate low Fe, Pb, and Zn contents with, in places, presence of chalcopyrite grains (Shepherd 2000 in Prodeminca 2000).

Fluid inclusions: results from this study

Data of 355 fluid inclusions are presented and discussed, of which 85 are from the study of Markowski et al. (2006). Data were collected on fluid inclusions from skarn samples ($n=244$) and from magmatic quartz of the potassic alteration zone and/or endoskarn in the Campanillas ($n=51$) and Fortuna ($n=44$) porphyritic intrusion, as well as from B veins related to K-alteration at Fortuna ($n=16$). Part of the data set has been preliminarily discussed by Fontboté et al. (2004).

Fluid inclusions of the skarn samples were investigated in skarn minerals (pyroxene, garnet, epidote, quartz), in calcite from vugs and type I veins, and in calcite from late faults of samples collected at Fortuna ($n=85$), Cambana ($n=34$), Campanillas ($n=44$), Nambija ($n=19$), and Guaysimi ($n=62$). Garnet of the dominant brown skarn is too opaque (in part due to the presence of titanium oxide needles) for fluid inclusion studies. No fluid inclusions could be analyzed from type II and type III veins due to their small size ($<3\ \mu\text{m}$).

In general, the fluid inclusions were difficult to characterize because they are both rare and small. An approach based on “Fluid inclusion assemblages” (Goldstein and Reynolds 1994) could not be applied. In addition, aberrant minimal temperature and trapping pressures and certain shapes (see below) suggest compositional and density re-equilibration. Despite these limitations, consistent fluid inclusion populations could be identified by selecting the most reliable data, on which the present study is based.

Fluid inclusions have been divided into five populations (Lh, Lc, L1, L2, and L3h) on the basis of host mineral, number of phases at room temperature, and microthermometric and Raman analysis (Figs. 4 and 5 and Tables 1 and 2). Below, a detailed description of each one of these populations is given.

Type Lh fluid inclusions

Halite-bearing *type Lh* fluid inclusions (Fig. 4a, b, c) occur in pyroxene from both green pyroxene-epidote skarn and endoskarn, in magmatic quartz of altered porphyritic intrusions, and rarely in quartz from B veins in porphyritic intrusions. They have diameters from 5 to 25 μm and contain up to five solid phases. In addition to halite, which typically crystallizes as cubes, sylvite and hematite have been identified (Fig. 4a, b). Other translucent, roundish, acicular, or hexagonal mineral phases could not be identified by Raman

spectrometry. Some of them melt at higher temperatures than the melting temperature of halite, and others are not affected by heating. They are possibly iron chlorides. Type Lh fluid inclusions in pyroxene and in fine-grained quartz of B veins are primary. Those in magmatic quartz from altered porphyritic intrusions are considered to be secondary. Type Lh fluid inclusions in magmatic quartz, and to a lesser extent in B vein quartz, show re-equilibration and necking down features (Fig. 4b, c) with variable vapor-to-liquid and liquid-to-salt ratios, the vapor bubble being occasionally absent. No microthermometric analyses could be carried out on fluid inclusions in pyroxene of the endoskarn because of the opacity of the mineral.

Melting temperatures of halite (\pm sylvite) indicate salinities between 30.9 and 65.6 wt.% eq. NaCl. The vapor bubble in pyroxene Lh fluid inclusions represents 10% to 30% of the inclusion volume. Most pyroxene Lh inclusions homogenize to the liquid phase by bubble disappearance between 412°C and $>600^\circ\text{C}$ (i.e., above the working limit of the fluid inclusion stage) with a strong mode between 430°C and 490°C (Fig. 5). Four fluid inclusions show temperature of bubble disappearance of $<400^\circ\text{C}$ and in one case halite dissolution occurs after the bubble disappearance at the final phase transition, suggesting necking down or re-equilibration processes.

In all studied Lh fluid inclusions in magmatic quartz from the altered porphyritic intrusions, bubble disappearance occurs before halite melting, between 107°C and 192°C. Most of them decrepitated before total homogenization, possibly due to the high internal pressure characteristic of homogenization by halite melting (Bodnar 1994). This feature, the extreme range of measured halite melting temperatures (187 to $\gg 450^\circ\text{C}$, which corresponds to 31.2 to $\gg 53$ wt.% eq. NaCl), and the low temperature of bubble disappearance all point to necking down and/or re-equilibration processes (Fig. 4b, c). Because of their small size, only one measurement could be made in Lh fluid inclusions from a B vein which gave a salinity of 65.6 wt.% eq. NaCl and a homogenization temperature of $>600^\circ\text{C}$.

Type Lc fluid inclusions

Type Lc consists of fluid inclusions in which CO_2 has been identified by microthermometry or Raman spectroscopy. Lc fluid inclusions include relatively CO_2 -rich inclusions in magmatic quartz (secondary, in part along fractures) and in B vein quartz (primary and secondary) of altered porphyritic intrusions. Another type of Lc primary fluid inclusions, which is characterized by very low CO_2 concentration (probably less than ~ 1 mol% since no phase transition involving CO_2 is observed by microthermometry, the CO_2 being only identified by Raman spectroscopy), occurs in endoskarn pyroxene (coexisting with primary Lh

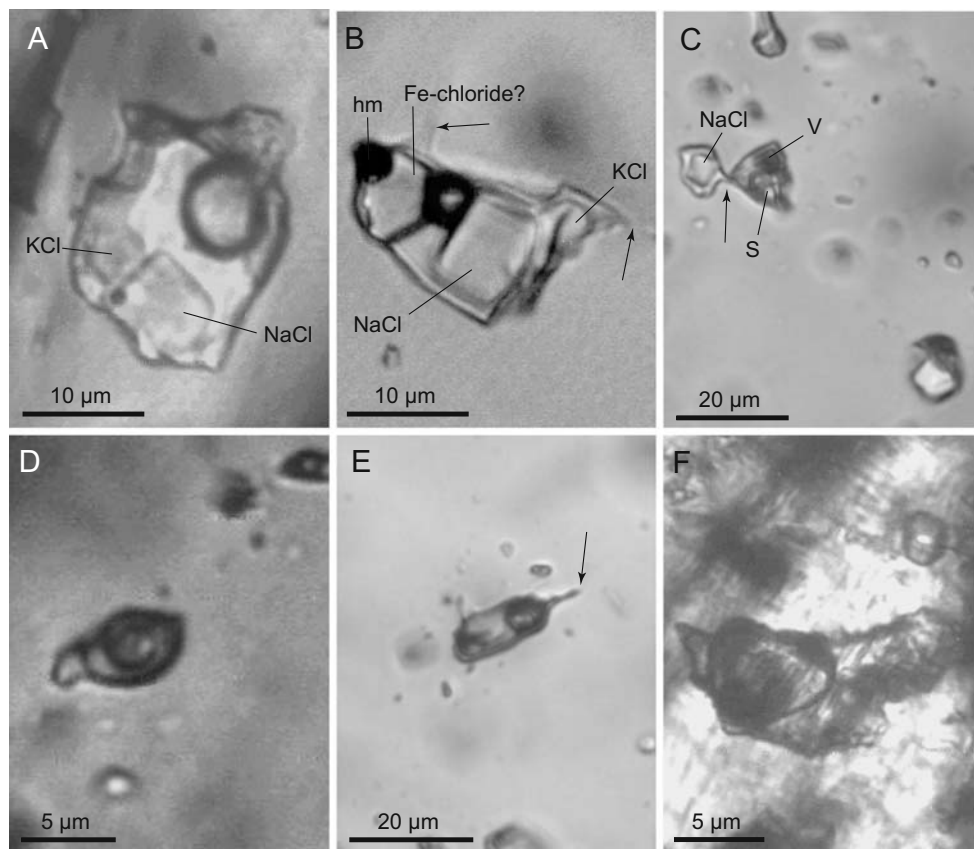


Fig. 4 Photomicrographs of the main fluid inclusion types. **a** Halite-bearing (NaCl) and sylvite-bearing (KCl) Lh fluid inclusion in pyroxene in blue–green garnet skarn (sample DTR135, Fortuna Cuerpo 3). **b** Multisolid (salts and hematite) Lh secondary fluid inclusions in magmatic quartz of the Campanillas altered porphyritic intrusion. The inclusions show sealed thin connecting tubes (*arrows*) typical for necking down phenomena. Note also a lower vapor-to-liquid ratio than in **a** (sample DTR69). **c** Halite-bearing Lh secondary fluid inclusions showing necking down in magmatic quartz of the Campanillas altered porphyritic intrusion. Necking down occurred

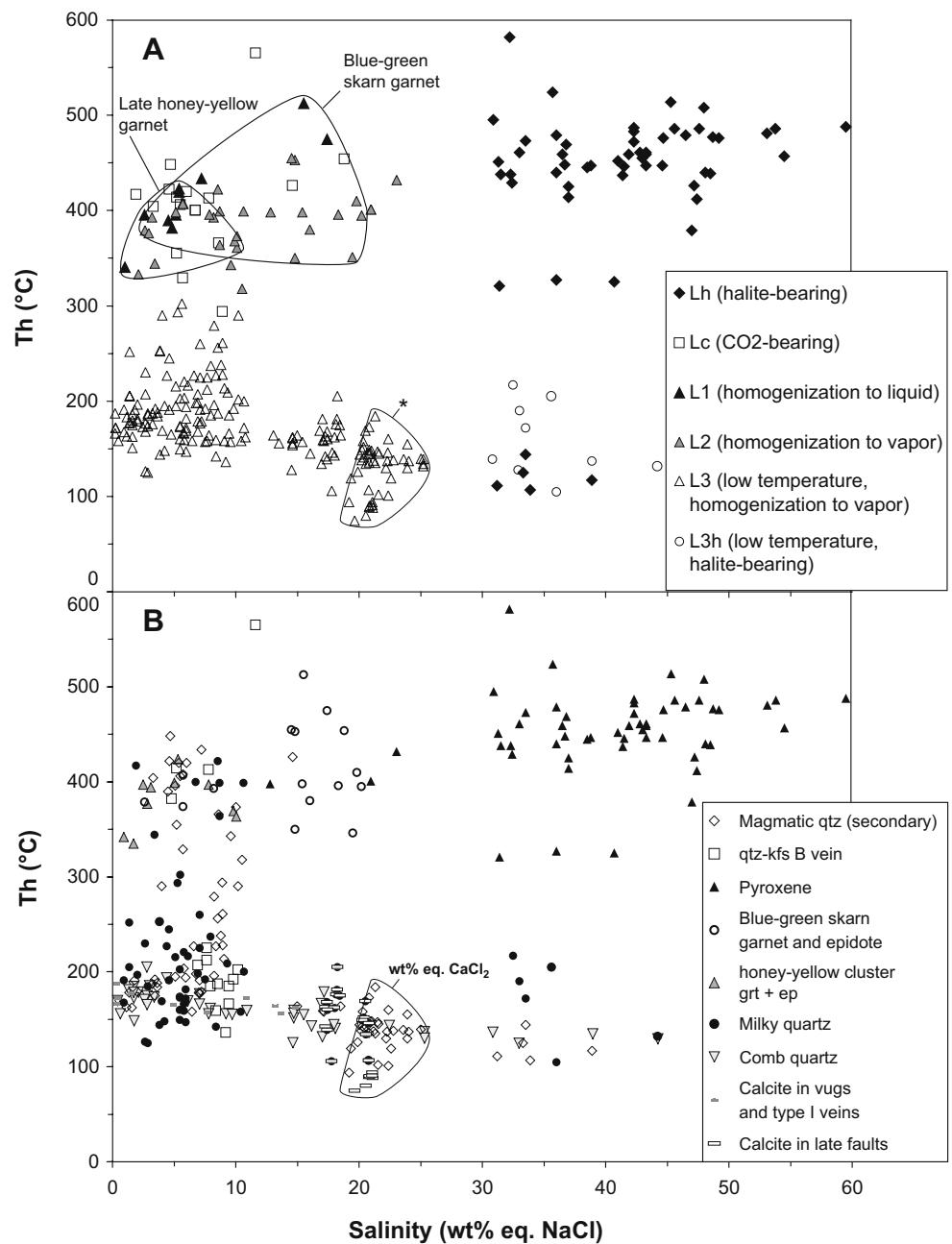
after the formation of the daughter crystals (sample DTR69). **d** High-density aqueous-carbonic Lc fluid inclusion in magmatic quartz of the Fortuna altered porphyritic intrusion (sample DTR64). **e** Aqueous-carbonic Lc fluid inclusion deformation of the walls (*arrow*) and a halo of small secondary fluid inclusions in magmatic quartz of the Campanillas altered porphyritic intrusion (sample DTR69). These features are typical for re-equilibration under conditions of internal underpressure. **f** Aqueous liquid-rich L1 fluid inclusion in garnet of the blue–green garnet skarn (sample DTR135, Fortuna Cuerpo 3)

inclusions), blue–green skarn garnet, and milky quartz of vugs and type I veins. The size of the Lc inclusions varies from 5 to 20 μm with a gas-to-liquid ratio between 0.2 and 1 and they do not contain any daughter mineral. A significant part of CO_2 -rich Lc fluid inclusions occurring in magmatic quartz and spatially associated with Lh inclusions shows re-equilibration and necking down features similar to those observed in Lh inclusions. An Lc fluid inclusion surrounded by clusters of small inclusions is shown in Fig. 4e. This feature is typical for re-equilibration under conditions of internal underpressure due to nearly isothermal compression or to isobaric cooling (Vityk and Bodnar 1995). The first process is unlikely to have occurred at Nambija since there are no indications of deformation that might suggest compression during the <1-My lifetime of the Nambija magmatic-hydrothermal system (Chiaradia et al. 2009).

Melting temperatures of CO_2 -rich phases are between -59.5°C and -57.7°C pointing to the presence of volatile species other than CO_2 . Melting temperatures of clathrate, when observable, range from -4.7°C to 10.7°C and CO_2 homogenization temperatures, when observable, range from -25°C to 29.9°C and occur to the gas or liquid phase.

Raman spectrometry analyses were conducted on 43 Lc fluid inclusions (Table 2). Among the volatile phases, CO_2 is dominant (with 94 to 100 mol%) and N_2 makes up to 6% of the volatile phase. H_2S was identified in 40% of the inclusions and traces of CH_4 were recorded in two fluid inclusions from magmatic quartz of the porphyritic intrusions. Modeling of bulk compositions of aqueous-carbonic fluid inclusions using melting temperature of ice and clathrate and homogenization temperature of the volatile phase indicate that water, CO_2 , and N_2 contents are in the range of 98.4 to 44.1, 55 to 1.6, and 1.3 to 0.0 mol%,

Fig. 5 Binary plots of temperature of liquid or vapor disappearance (Th) vs. salinity. **a** Data ordered by fluid inclusions type (nomenclature is explained in the text). **b** Same data ordered by host mineral. Earlier aqueous-carbonic fluid inclusions are not presented as their high internal density resulting from necking down leads to decrepitation before total homogenization. *Asterisk*, for this field, the CaCl_2 equivalent instead of NaCl equivalent has been plotted for fluid inclusions in calcite, comb quartz, and secondary fluid inclusions in magmatic quartz of this field



respectively, with salinities between 20 and 1.9 wt.% eq. NaCl. The bulk composition of type Lc fluid inclusions, for which not all microthermometric parameters could be measured because of low volatile content or poor conditions of observation, was calculated ignoring salts. Type Lc fluid inclusions affected by necking down in the magmatic quartz of the altered porphyritic intrusions show strong dispersion of densities and CO_2 contents, and most of them decrepitate before homogenization. Total homogenization occurs to the liquid, critical, or vapor phase between 565°C and 294°C . Fluid inclusions showing the highest temperature homogenize to the vapor phase and occur in magmatic quartz of the altered porphyritic

intrusions and in B veins. It should be noted that fluid inclusions showing re-equilibration features were observed only in the magmatic quartz and to a lesser extent in B veins and in pyroxene of the pyroxene-epidote skarn, i.e., re-equilibrated fluid inclusions appear to be the “oldest” and trapped at the highest temperatures.

Some Lc inclusions have CO_2 contents so low that it was only identified by Raman spectroscopy. These CO_2 -poor inclusions do not show re-equilibration or necking down features and frequently occur together with two-phase aqueous fluid inclusions, in particular in garnet of the blue-green skarn, suggesting that there is a transition between Lc and L1/L2 fluid inclusions.

Table 1 Summary of microthermometric data of fluid inclusions from the Nambija skarn deposits

Stage	Fluid inclusion type	Host mineral	Location	Number	Microthermometric data									
					Tm CO ₂ (°C)	Th CO ₂ (°C)	Tm ice (°C)	Tm cl (°C)	Tm NaCl (°C)	Tm KCl (°C)	Th L–V (°C)	Th total (°C)	Salinity	
Prograde stage	Lh high-temperature, halite bearing	Pyroxene ^a , B vein quartz	Fortuna, Cambana, Nambija-El Playon, Nambija-El Tierrero	48	–	–	–26 to –49	–	–	542 to 180	107 to 53	>600 to 412	>600 to 412	65.6 to 30.9 wt.% eq. NaCl
	Lh with possible necking down	Pyroxene, magmatic quartz ^b	Fortuna, Cambana, Campanillas	9	–	–	–	–	–	>450 to 187	–	379 to 107	>450 to 187	>53 to 31.2 wt.% eq. NaCl
Prograde stage and retrograde stage over 310°C	Lc high to intermediate temperature, CO ₂ bearing	Magmatic quartz ^a , B vein quartz, blue-green skarn garnet, milky quartz	Fortuna, Campanillas, Guaysi	34	–57.7 to –59.5	29 to –25	–1.1 to –15.2	8.2 to –4.7	–	–	–	565 to 294	565 to 294	18.8 to 1.9 wt.% eq. NaCl
	Lc with possible necking down	Magmatic quartz ^b	Fortuna	9	–58.1 to –59.3	29.8 to 27	–	10.7 to –1.5	–	–	–	420, 443 ^c	420, 443 ^c	20 to 4.3 wt.% eq. NaCl
L1 intermediate temperature, vapor rich, aqueous	L1 intermediate temperature, liquid rich, aqueous	Blue-green skarn and blue-green skarn and cluster epidote, milky quartz, B vein quartz, and magmatic quartz ^b	Fortuna, Campanillas, Nambija-El Tierrero, Guaysimi	11	–	–	–0.6 to –13.6	–	–	–	–	513 to 341	513 to 341	17.4 to 1.0 wt.% eq. NaCl
			Fortuna, Cambana, Campanillas, Nambija-El Playon, Nambija-El Tierrero, Guaysimi	32	–	–	–1.2 to –21	–	–	–	–	–	455 to 318	455 to 318
Retrograde stage below 310°C	L3 low temperature, liquid rich, aqueous	Comb quartz, calcite from yug, milky quartz ^b , B vein quartz ^b , and magmatic quartz ^b	Fortuna, Campanillas, Guaysimi	169	–	–	–0.1 to –31	–	–	–	–	302 to 94	302 to 94	23 to 0.2 wt.% eq. NaCl
			Fortuna, Campanillas	9	–	–	–	–	–	–	>420 to 175	–	217 to 105	>420 to 175
Late faults	L3 low temperature, liquid rich, aqueous	Calcite in late fault	Guaysimi	34	–	–	–	–	–	–	–	205 to 74.5	205 to 74.5	21.1 to 17.3 wt.% eq. NaCl
			Fortuna, Campanillas	–	–	–	–	–	–	–	–	–	–	–

Fluid inclusion types are defined in the text. *Italic* denotes necking down

*Tm*CO₂ melting temperature of solid CO₂, *Th* CO₂ homogenization temperature of CO₂, *Tm ice* melting temperature of ice, *Tm cl* melting temperature of clathrate, *Tm NaCl* melting temperature of halite, *Tm KCl* melting temperature of sylvite, *Th L–V* temperature of liquid or vapor bubble disappearance

^a Always primary

^b Always secondary

^c Only two values most of the fluid inclusions decrepitate before homogenization

^d Salinities were calculated in the H₂O–CaCl₂ system when Tm ice is below –21.1°C

Table 2 Chemical compositions obtained by Raman spectroscopy of selected fluid inclusions and corresponding microthermometric data, from the Nambija skarn deposits

Sample and reference inclusion	Host mineral	Microthermometry				Volatile phase				Density				NaCl (wt. %)								
		CO ₂		ice		Th	Mode	Th	Mode	%	vol.		CO ₂		CH ₄		N ₂		NaCl			
		Tm	Cl	Tm	Cl						CO ₂	CH ₄	N ₂		H ₂ S	H ₂ O	CO ₂	CH ₄		N ₂	NaCl	
DTR64-8136-2.1.1	Magmatic quartz ^a	-58.9	no	no	no	27.3	L	27.3	L	100	95.3	0.0	4.7	-	0.70	0.0	95.3	0.0	4.7	0.0	0.0	0.70
DTR64-8137-2.1.1		-58.2	no	-1.5	no	29.5	V	>250	L	20	97.5	0.0	2.5	-	0.26	88.3	5.0	0.0	0.0	6.7	20.0	0.94
DTR64-8137-3.1.1		-58.1	no	5.1	no	29.0	L	>240	no	40	98.4	0.0	1.6	X	0.55	78.5	18.6	0.0	0.3	2.6	9.5	0.89
DTR64-8137-3.2.1		-58.2	no	10.7	no	29.8	L	d	-	30	100.0	0.0	0.0	X	0.66	87.4	12.6	0.0	0.0	0.0	0.0	0.88
DTR64-8137-3.3.1		-59.3	no	2.9	no	29.4	L	d	-	80	98.3	0.0	1.7	-	0.55	43.2	53.9	0.0	0.9	2.0	13.2	0.76
DTR184a-1.1.1		-58.9	no	8.1	no	29.9	L	>270	-	40	97.4	0.0	2.6	X	0.56	80.2	18.3	0.0	0.4	1.1	4.3	0.88
DTR184a-1.2.2		-58.5	no	2.1	no	no	no	443	C	20	98.5	0.0	1.5	-	0.03	98.0	2.0	0.0	0.0	0.0	0.0	0.83
DTR184a-1.2.6		-59.3	no	2.9	no	27.0	V	d	-	20	97.7	0.0	2.3	-	0.23	90.7	5.0	0.0	0.1	4.2	13.1	0.92
DTR184a-1.4.1		-59.3	no	7.3	no	28.4	L	420	V	30	96.4	0.0	3.6	-	0.58	84.4	13.6	0.0	0.4	1.6	6.0	0.92
DTR64-8136-2.2.1		-59.1	no	no	no	21.0	V	21.0	V	100	97.5	0.0	2.5	X	0.21	0.0	97.5	0.0	2.5	0.0	0.0	0.21
DTR64-8136-2.2.3		-58.3	no	no	no	-25.0	V	-25.0	V	100	99.4	0.0	0.6	X	0.04	0.0	99.4	0.0	0.6	0.0	0.0	0.04
DTR64-8136-2.2.6		no	no	no	no	-5.0	V	-5.0	V	100	99.0	0.0	1.0	X	0.09	0.0	99.0	0.0	1.0	0.0	0.0	0.09
DTR64-8137-1.1.1		-58.9	no	7.2	no	21.0	V	329	V	70	94.3	0.0	5.7	X	0.16	81.7	15.8	0.0	0.8	1.7	5.8	0.42
DTR64-8137-1.1.2		-58.7	no	6.5	no	12.8	V	>270	V	70	100.0	0.0	0.0	-	0.15	82.6	15.6	0.0	0.0	1.8	6.6	0.41
DTR64-8137-1.2.1		-58.9	no	5.3	no	21.4	V	294	V	70	99.4	0.0	0.6	X	0.20	77.5	20.2	0.0	0.1	2.2	8.9	0.46
DTR64-8137-1.3.1		-59.3	no	no	no	22.0	V	22.0	V	100	97.9	0.0	2.1	X	0.22	0.0	97.9	0.0	2.1	0.0	0.0	0.22
DTR64-8137-1.3.2		-58.9	no	no	no	21.0	V	d	-	100	98.8	0.0	1.2	-	0.21	0.0	98.8	0.0	1.2	0.0	0.0	0.21
DTR64-8137-2.2.1		-57.7	no	1.9	no	29.0	V	426	L	50	98.4	0.0	1.6	-	0.26	82.7	12.7	0.0	0.2	4.4	14.6	0.68
DTR69-5.2.1		no	no	no	no	no	no	371	V	70	98.1	0.0	1.9	X	nc	nc	nc	nc	nc	nc	nc	nc
DTR184a-1.2.1		-58.1	no	-5.1	no	no	no	406	C	40	98.5	0.0	1.5	X	0.04	95.4	2.9	0.0	0.0	1.7	5.5	0.62
DTR184a-1.2.5		-58.3	no	4.5	no	no	no	447	C	30	97.3	0.0	2.7	-	0.04	97.3	2.7	0.0	0.0	0.0	0.0	0.73
DTR184a-1.4.4		-59.5	no	7.5	no	no	no	406	V	30	97.0	0.3	2.7	-	0.06	96.5	3.5	0.0	0.0	0.0	0.0	0.72
DTR184a-1.6.1		no	no	5.5	no	no	no	397	C	50	99.0	0.0	1.0	X	0.05	96.0	4.0	0.0	0.0	0.0	0.0	0.52
DTR184a-2.1.3		no	no	3.9	no	no	no	427	V	70	94.8	0.0	5.2	-	0.04	94.4	5.4	0.0	0.2	0.0	0.0	0.34
DTR184a-2.1.7		no	no	8.2	no	no	no	405	V	60	100.0	0.0	0.0	-	0.07	93.5	6.5	0.0	0.0	0.0	0.0	0.46
DTR184a-2.1.8		-58.4	no	6.9	no	no	no	506	V	50	99.3	0.0	0.7	X	0.06	95.5	4.5	0.0	0.0	0.0	0.0	0.55
DTR184a-2.1.10		no	no	4.1	no	no	no	468	V	50	98.2	0.0	1.8	-	0.04	96.5	3.5	0.0	0.0	0.0	0.0	0.53
DTR184a-2.1.13		no	no	-5.0	no	no	no	448	V	50	97.7	0.0	2.3	-	0.05	94.3	4.2	0.0	0.1	1.4	4.7	0.55
DTR184a-2.1.14		no	no	-5.0	no	no	no	422	V	50	97.0	0.0	3.0	X	0.06	94.2	4.3	0.0	0.1	1.4	4.6	0.55
DTR184a2.1.16		no	no	-4.0	no	no	no	404	V	40	100.0	0.0	0.0	X	0.07	94.6	4.4	0.0	0.0	1.0	3.3	0.66
DTR184a-1.2.4		-58.9	no	5.1	no	no	no	407	L	30	96.1	0.0	3.9	-	0.05	97.2	2.8	0.0	0.0	0.0	0.0	0.71
DTR184a-1.6.3		-59.2	no	5.5	no	14.5	V	366	L	50	97.0	0.0	3.0	X	0.16	88.0	9.2	0.0	0.2	2.6	8.6	0.60
DTR184a-2.1.1		no	no	-2.0	no	no	no	355	L	30	97.0	0.0	3.0	X	0.02	96.8	1.6	0.0	0.0	1.6	5.2	0.72

DTR184b-1.4.1	no	-7.4	3.1	no	no	413	V	40	97.6	0.0	2.4	-	0.06	93.8	3.7	0.0	0.1	2.4	7.8	0.66
DTR184b-1.4.2	no	-4.5	-4.7	no	no	414	V	50	98.6	0.0	1.4	-	0.02	96.3	2.1	0.0	0.0	1.6	5.2	0.52
DTR184b-1.4.3	no	-5.4	-1.4	no	no	>520	V	40	98.2	0.0	1.8	-	0.03	95.7	2.5	0.0	0.0	1.8	5.9	0.62
DTR184b-1.4.4		no	3.5	no	no	399	C	40	100.0	0.0	0.0	-	0.04	97.2	2.8	0.0	0.0	0.0	0.0	0.63
DTR184b-2.2.2	B vein quartz	-58.1	no	no	no	d	-	100	96.4	0.0	3.6	-	nc	0.0	96.4	0.0	3.6	0.0	0.0	nc
DTR184b-2.2.4		-58.0	no	no	no	d	-	100	96.2	0.0	3.8	-	nc	0.0	96.2	0.0	3.8	0.0	0.0	nc
DTR184b-2.2.5		-58.0	no	3.7	5.0	V	565	50	98.4	0.0	1.6	-	0.11	89.1	7.3	0.0	0.0	3.6	11.6	0.60
DTR 136-3.1.3	BGSK garnet** milky quartz	no	-15.2	no	no	no	L	30	92.7	0.0	7.3	-	nc	nc	nc	nc	nc	nc	18.8	0.71
DTR365-2-2.1.11		no	-1.1	no	no	no	V	60	94.0	0.0	6.0	-	nc	nc	nc	nc	nc	nc	1.9	0.48
DTR365-2-2.1.13		no	-4.2	no	no	no	V	70	94.9	0.0	5.1	X	nc	nc	nc	nc	nc	nc	6.7	0.57

Compositions are given in mole percent. All values are in degree Celsius. CO₂ detected only by Raman spectroscopy. Fluid inclusions where both T_m ice and ThCO₂ could not be measured had to be modeled without electrolytes (i.e., 0 wt.% eq. NaCl)

T_mCO₂, melting temperature of solid CO₂, Th CO₂ homogenization temperature of CO₂, T_m ice melting temperature of ice, T_m cl melting temperature of clathrate, Th homogenization temperature, L liquid, C critical, V vapor. *Italic Th values* decrepitation, d non-observed due to decrepitation, no not observed, X presence of H₂S, nc not computable and considered as aqueous fluid inclusion

^a Always secondary

^b Blue-green skarn garnet

Type L1 fluid inclusions

Type L1 fluid inclusions are vapor-rich two-phase aqueous fluid inclusions that homogenize to the vapor or critical phase between 513°C and 341°C. They occur in magmatic quartz of the altered porphyritic intrusions, in endoskarn pyroxene, in quartz of the B veins, in garnet and epidote from clusters and blue-green skarn, and in milky quartz of vugs and type I veins. They are primary in garnet, epidote, and milky quartz of vugs and type I veins and secondary in magmatic quartz of the altered porphyritic intrusions. Salinities range from 17.4 to 1.0 wt.% eq. NaCl and initial melting of ice below -21.1°C indicates the presence of significant amounts of cations other than Na⁺. The highest homogenization temperatures and salinities were encountered in blue-green skarn garnet.

Type L2 fluid inclusions

Type L2 fluid inclusions are two-phase liquid-rich aqueous fluid inclusions with vapor-to-liquid ratio between 0.2 and 0.5 having homogenization temperatures to the liquid phase in the range of 455°C to 318°C and salinities in the range of 23 to 2.1 wt.% eq. NaCl. They occur in magmatic quartz of the altered porphyritic intrusions, in B vein quartz, in pyroxene, in late garnet and epidote from clusters (Fig. 4f) and blue-green skarn, and in milky quartz of vugs and type I veins. Type L2 fluid inclusions are primary in pyroxene, late garnet, and epidote from clusters (Fig. 4f) and blue-green skarn and in part in milky quartz of vugs and type I veins. Type L2 fluid inclusions in magmatic quartz of the altered porphyritic intrusions and most of those occurring in milky quartz of vugs and type I veins are secondary. Occasionally, L2 fluid inclusions contain a translucent solid that does not melt during heating and was identified as calcite by Raman spectroscopy. Initial melting of ice below -21.1°C indicates the presence of significant amounts of cations other than Na⁺.

Type L3 fluid inclusions

Type L3 are two-phase liquid-rich aqueous fluid inclusions with low vapor content (vapor-to-liquid ratio around 0.05) and homogenization temperatures below 300°C. They constitute the most abundant fluid inclusion type and occur in all fluid-inclusion-bearing minerals except calc-silicates. They are primary only in late comb quartz and in cavities- and vein-filling calcite as well as in calcite sealing late normal faults. Type L3 fluid inclusions show initial melting temperature of ice below -21.1°C and up to -52°C, which is the eutectic of the H₂O-NaCl-CaCl₂ system. Final melting temperatures of ice are between -31°C and -0.1°C. Salinities of fluid inclusions having melting temperature of ice between -21.1°C and -31°C have been calculated in

the H₂O–CaCl₂ system. Thus, salinities range from 23.5 to 0.2 wt.% eq. NaCl and from 25.2 to 21.3 wt.% eq. CaCl₂. Type L3 fluid inclusions homogenize to the liquid phase in the range of 302°C to 74.5°C, the lowest Th and highest salinities typically being found in calcite from late faults (Figs. 5 and 6). These L3 fluid inclusions are similar to those analyzed by Shepherd (1988 in Litherland et al., 1994; 2000 in Prodeminca 2000; personal communication 2003).

Halite-bearing (up to 30% in volume) two-phase liquid-rich aqueous fluid inclusions have been defined as subtype L3h. They are recognized only at Fortuna and Campanillas, where they occur as primary fluid inclusions in comb quartz and in fractures together with L3 fluid inclusions, in magmatic quartz of the altered porphyritic intrusions, and

in milky quartz of vugs and type I veins. Vapor-to-liquid ratio is the same as in the L3 fluid inclusions (around 0.05). On heating, the vapor bubble disappears between 95°C and 217°C and total homogenization occurs by halite dissolution between 175°C and >420°C, which corresponds to salinities between 30.8 and >50 wt.% eq. NaCl. Similar to Lh inclusions in magmatic quartz of the altered porphyritic intrusions, most of the L3h fluid inclusions decrepitate before total halite dissolution due to internal overpressures.

Chlorite thermometry

Chlorite is the most abundant Mg- and Fe-bearing phase of the retrograde mineral assemblage and replaces both

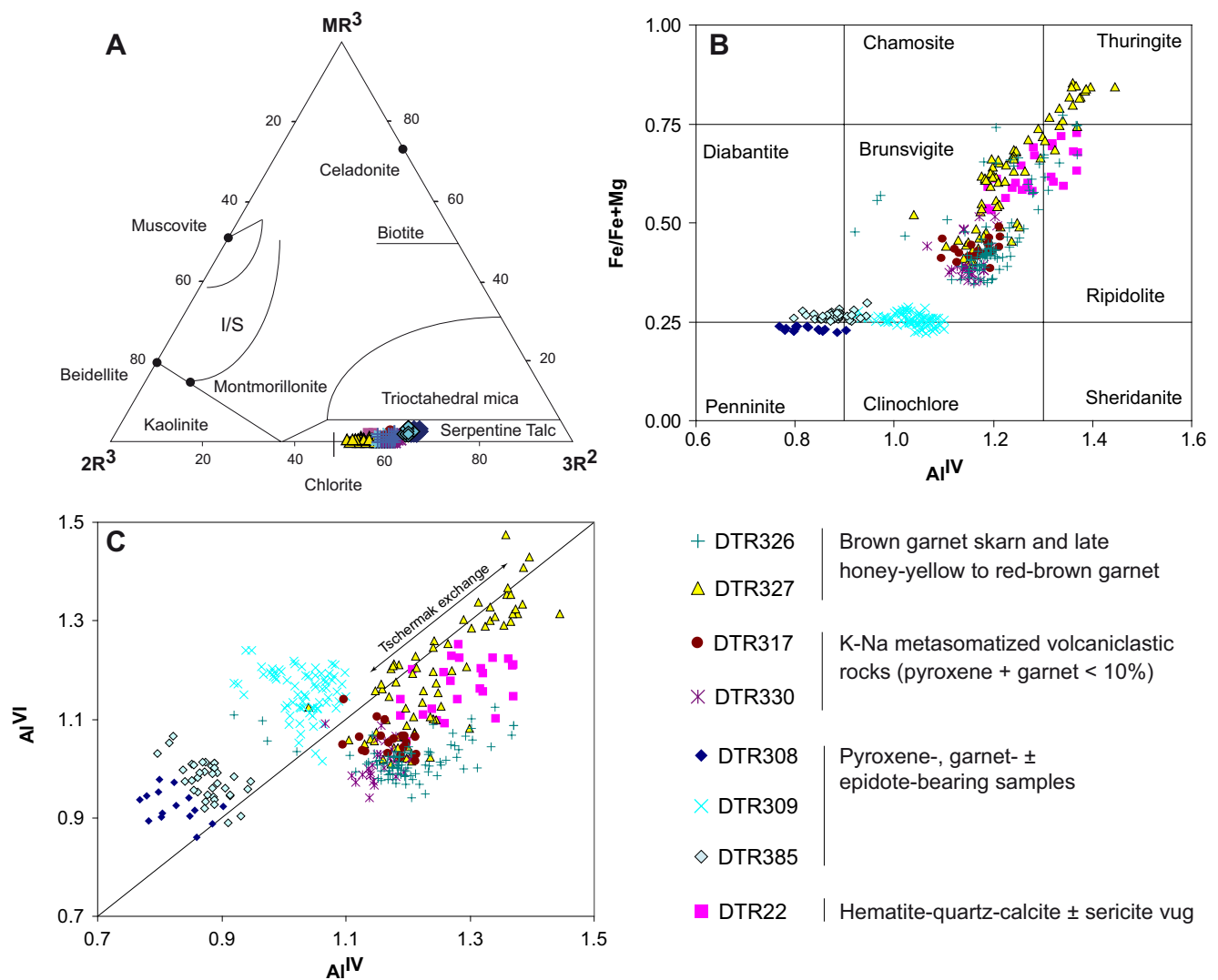


Fig. 6 Chlorite geochemistry. **a** Triangular plot of Velde (1985) showing that almost all analyses plot in the field of chlorite (chlorite of samples DTR308 and DTR385 exhibits some Ca). *I/S* interstratified illite/smectite. $MR3 = K + Na + 2Ca$, $2R3 = (Al - (K + Na + 2Ca)) / 2$,

$3R2 = Fe + Mg + Mn / 3$. **b** Iron number vs. silica classification diagram of Foster (1962). **c** Octahedral alumina (Al^{VI}) vs. tetrahedral alumina plot (Al^{IV})

pyroxene and garnet. It is finely intergrown with gold and calcite, suggesting a coeval formation with the latter. Under the optical microscope, the color of chlorite ranges from pale yellow to dark green reflecting variations in the Fe content, as previously noted at Fortuna (Markowski et al. 2006). Microprobe analyses were carried out on retrograde chlorite to calculate formation temperatures using chlorite geothermometers (Cathelineau 1988, Jowett 1991). To avoid calcite contamination, only samples with relatively coarse-grained chlorite were selected from Cambana (DTR308, DTR309) and Campanillas (DTR22, DTR327, and DTR330; see Fig. 7 and Table 3). Chlorite structural formulae were calculated on the basis of 14 oxygens.

In Velde’s (1985) diagram (Fig. 7a), all samples plots in the chlorite field, except samples DTR308 and DTR385, in which Ca contents are up to 0.04 cations point to a smectite component. In Foster’s (1962) diagram, two chlorite groups can be distinguished on the basis of chlorite Fe number and the occurrence of chlorite in association or not with pyroxene (Fig. 7):

- Chlorite in pyroxene-bearing samples (DTR308, DTR309, and DTR385) has low Fe numbers (0.22 to 0.3) and relatively high silica content with no correla-

tion between Fe number and Si. Manganese content varies from 0.13 to 0.26 cations. Chlorite from samples DTR308 and DTR385 contains up to 0.4 wt.% CaO indicating the presence of a smectite component.

- Chlorite in pyroxene-free samples with variable garnet contents (DTR22, DTR317, DTR326, DTR327, and DTR330) has Fe numbers ranging from 0.35 to 0.86, with variations also within single grains (samples DTR326 and DTR327; Figs. 2f and 7). The Fe numbers correlate positively with tetrahedral alumina (Al^{IV}). Manganese cation numbers vary from 0.62 to 3.10 and correlate weakly with iron and total alumina.

The same two groups are distinguished on the basis of the ratio of Al^{VI} to Al^{IV} . In chlorite of pyroxene-free samples, Al distribution (Fig. 7c) is governed by the “Tschermak exchange” ($Mg^{VI}Si^{IV} \leftrightarrow Al^{VI}Al^{IV}$). The pyroxene-bearing samples DTR308 and DTR309, however, show a negative correlation between the tetrahedral and octahedral alumina (Fig. 7c), and tetrahedral Al distribution is a function of vacancies in the octahedral site.

Cathelineau’s (1988) and Jowett’s (1991) geothermometers are based on the tetrahedral alumina content, which, in principle, increases with temperature. The chlorite

Fig. 7 a Plot of oxygen isotope compositions of quartz and calcite from the Nambija skarns. Oxygen isotope compositions of the depositing fluids are calculated using the fractionation equations of Matsuhisa et al. (1979) for quartz and O’Neil et al. (1969) for calcite using temperatures deduced from the fluid inclusion study. Field of primary magmatic water is from Sheppard (1986). **b** Plot of the $\delta^{13}C$ and $\delta^{18}O$ values of calcite from comb quartz cavities and veins and calcite in late faults. Fields of igneous calcite and marine limestone are from Bowman (1998)

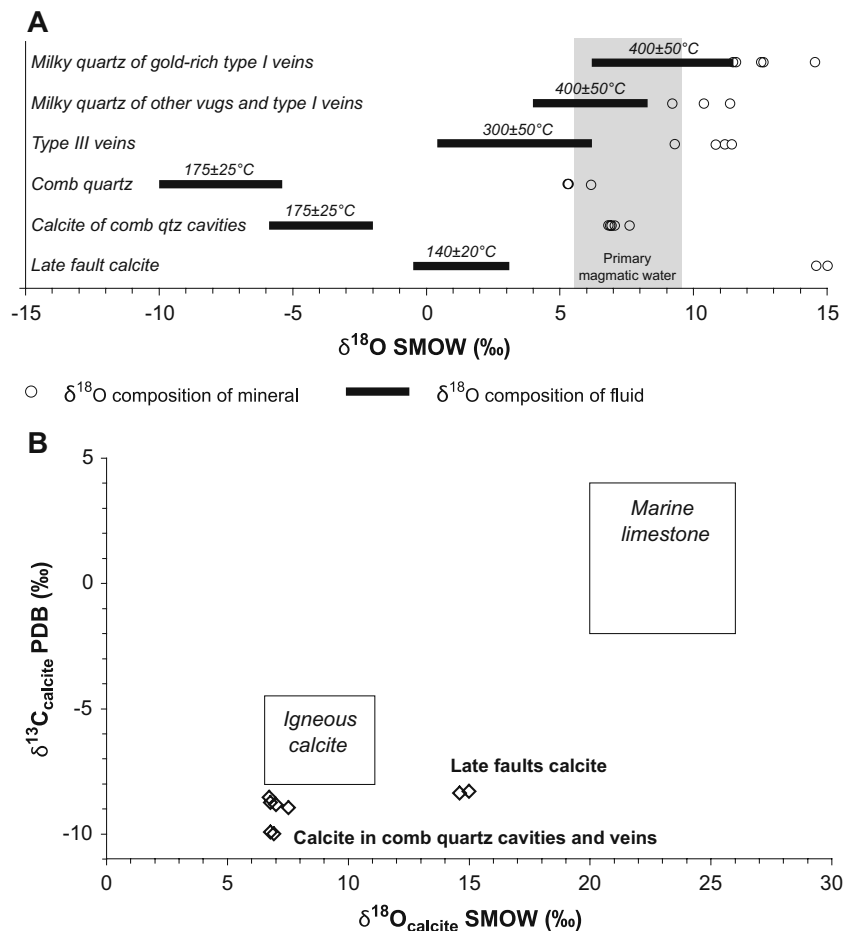


Table 3 Microprobe analyses and calculated formation temperature of representative various chlorite parageneses from the Nambija district

Sample label location	DTR 327 4_16 Campanillas mine	DTR 327 6_11	DTR 22 3_3	DTR 22 1b_2	DTR 317 1_4	DTR 330 3_4	DTR 385 3_10	DTR 309 4_12 Cambana mine	DTR 308 3_4
	Strongly zoned chlorite in vugs from brown garnet skarn		Vug filled by chlorite, quartz, hematite, calcite, and sericite		Chlorite replacing grt in KNa metasomatized volcaniclastic rocks		Chlorite replacing px in blue–green garnet skarn	Chlorite in type II vein in the green pyroxene- epidote skarn	Chlorite in post- ore veinlets in green pxep skarn
SiO ₂	23.53	28.32	25.95	24.07	27.04	27.86	30.71	30.55	32.17
Al ₂ O ₃	20.51	19.41	18.24	18.76	18.17	18.33	15.62	19.43	15.07
FeO	39.17	21.35	29.65	29.95	21.40	19.15	15.15	13.70	13.79
MgO	3.73	18.32	11.63	11.57	16.90	19.60	23.15	23.60	25.25
MnO	3.60	3.24	3.28	3.48	4.03	4.13	2.35	2.41	1.72
CaO	0.03	0.04	0.05	nd	0.09	nd	0.14	0.10	0.26
Na ₂ O	nd	nd	0.05	nd	nd	nd	0.01	nd	nd
K ₂ O	0.02	nd	0.11	0.02	0.02	0.01	0.01	nd	0.01
TiO ₂	0.02	0.03	nd	0.11	0.04	nd	nd	nd	0.01
H ₂ O ^a	9.4	9.3	11.1	12.1	12.3	10.9	12.9	10.2	11.7
Total	100.0	100.0	100.0	100.0	100.0	100.0	100.0	100.0	100.0
Structural formula on the basis of 14 oxygens									
Si	2.64	2.85	2.81	2.66	2.85	2.85	3.11	2.97	3.17
Al ^{IV}	1.36	1.15	1.19	1.34	1.15	1.15	0.89	1.03	0.83
Al	2.71	2.31	2.33	2.44	2.26	2.21	1.86	2.22	1.75
Al ^{VI}	1.35	1.16	1.14	1.10	1.11	1.06	0.97	1.19	0.93
Fe	3.68	1.80	2.69	2.77	1.89	1.64	1.28	1.11	1.14
Mg	0.62	2.75	1.88	1.90	2.65	2.99	3.49	3.41	3.71
Mn	0.34	0.28	0.30	0.33	0.36	0.36	0.20	0.20	0.14
Ca	0.00	0.00	0.01	0.00	0.01	0.00	0.01	0.01	0.03
Na	0.00	0.00	0.01	0.00	0.00	0.00	0.00	0.00	0.00
K	0.00	0.00	0.01	0.00	0.00	0.00	0.00	0.00	0.00
Ti	0.00	0.00	0.00	0.01	0.00	0.00	0.00	0.00	0.00
Fe/(Fe + Mg)	0.86	0.40	0.59	0.59	0.42	0.35	0.27	0.25	0.23

Conditions of probe analyses are 15 nA for beam current and 15 kV for acceleration voltage. All iron is calculated as ferrous
nd not detected

^a H₂O calculated by difference from 100%

geothermometer can be applied only if no smectite layers are intergrown with chlorite and for chlorite with Fe numbers <0.6. The chlorite of samples DTR308 and DTR385 contains smectite layers and is, therefore, unsuitable for geothermometry. Likewise, chlorite from pyroxene-free samples cannot be used as a geothermometer because its Al distribution is governed by the Tschermak exchange and does not reflect the formation temperature (Cathelineau personal communication 2007). Sample DTR309 is the only sample meeting the criteria for chlorite geothermometry. However, correlation between tetrahedral and octahedral alumina is poor (Fig. 7c) casting doubts on the calculated temperatures. Chlorite analyzed by Markowski et al. (2006) at Fortuna shows a similar pattern, with increasing Fe number and with

increasing tetrahedral alumina and Al distribution governed by the Tschermak exchange. The same concerns on the validity of the chlorite geothermometer may apply for the temperatures published by Hammarstrom (1992) on Nambija samples.

Stable isotope geochemistry

Samples and analytical techniques

Oxygen isotope compositions were measured for milky quartz from vugs and type I veins, for quartz of type III veins, and for comb quartz of cavities and veins. Carbon

and oxygen isotope compositions of calcite from comb quartz cavities and veins and calcite in late faults were also measured.

Milky quartz of vugs and type I veins

The $\delta^{18}\text{O}$ values of milky quartz of vugs and type I veins vary from 14.6‰ to 9.2‰ (Fig. 8a and Table 4). Milky quartz in samples from gold-rich type I veins has higher $\delta^{18}\text{O}$ values (14.6‰ to 11.5‰) than milky quartz of gold-poor vugs and type I veins (11.3‰ to 9.2‰). The temperature of milky quartz deposition is estimated at 450°C to 350°C on the basis of the fluid inclusion study. Using the fractionation equation of Matsuhisa et al. (1979) and quartz deposition temperatures estimated at 450°C to 350°C on the basis of the fluid inclusion studies, the calculated $\delta^{18}\text{O}$ values of water in equilibrium with milky quartz of gold-rich type I veins are 6.2‰ to 11.5‰. Slightly lower $\delta^{18}\text{O}_{\text{water}}$ values (4.0‰ to 8.3‰) are obtained for milky quartz depositing fluids in other vugs and type I veins (Fig. 8a and Table 4).

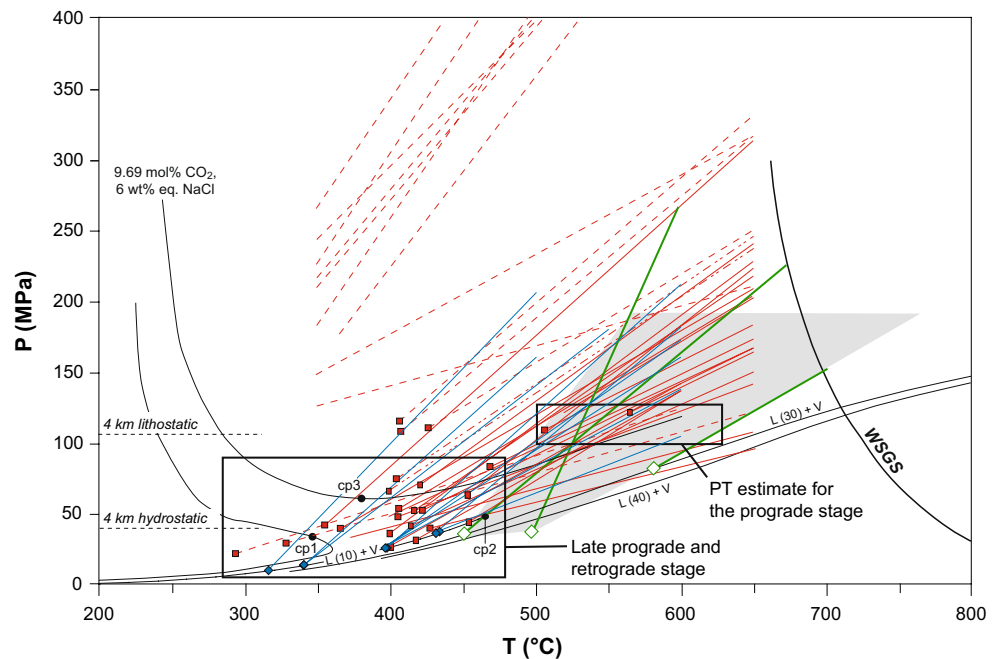
Type III vein quartz

Type III vein quartz has $\delta^{18}\text{O}$ values between 11.5‰ and 9.3‰ (Fig. 8a and Table 4), the molybdenite-bearing sample DTR358 of the El Tierrero mine having the lowest value (Table 4). It is difficult to constrain the formation temperature of type III veins as no analyzable fluid inclusions have been found. However, as type III veins are assigned to the retrograde alteration because of their chlorite, sericite, epidote, and calcite assemblage, a formation temperature between 250°C and 350°C has been assumed. The calculated equilibrium $\delta^{18}\text{O}_{\text{water}}$ values of fluids that formed the quartz are between 0.4‰ and 6.2‰ (Fig. 8a and Table 4).

Late comb quartz and calcite filling cavities and veins

Two comb quartz samples in late assemblages of quartz, \pm chlorite, \pm calcite, and \pm hematite filling cavities and veins have $\delta^{18}\text{O}$ values of 6.2 (clear comb quartz, Figs. 2e and 8a and Table 4) and 5.3 (purple comb quartz, Fig. 8a and

Fig. 8 Pressure–temperature plot of the isochores of all Lc aqueous-carbonic fluid inclusions and of four selected Lh halite-bearing fluid inclusions. The field of isochores of Lh inclusions with homogenization temperatures over 450°C is also represented. Isochores of Lc aqueous-carbonic fluid inclusions showing necking down features (dashed lines) are generally steep and indicate unrealistically high pressures. See detailed explanation in text. WSGS water saturated granodiorite solidus



- Isochore of Lc fluid inclusions
- - - Isochore of Lc fluid inclusions showing necking down or reequilibration features
- · - · Isochore of possibly reequilibrated Lc fluid inclusions
- Lc fluid inclusion homogenization temperature
- Isochore of Lh fluid inclusions
- ◇ Lh fluid inclusion homogenization temperature
- Isochore of selected L1 and L2 fluid inclusions
- ◆ L1 and L2 fluid inclusion homogenization temperature

cp1: critical point for the mixture 10 mol% CO₂ + 90 mol% H₂O (Takenouchi and Kennedy 1964)

cp2: critical point for a 10 wt% eq NaCl aqueous fluid (Knight and Bodnar 1989)

cp3: critical point for the mixture 9.69 mol% CO₂ + 88.57 mol% H₂O + 1.74 mol% NaCl or 6 wt% NaCl (Diamond 2003)

L-V curves (with salinities in wt% eq. NaCl in parenthesis) are from Khaibullin and Borisov (1966) and Bodnar et al. (1985)

Table 4 Summary of oxygen isotope compositions for quartz and of oxygen and carbon isotope compositions for calcite of the Nambija district deposits

Mineral	Sample	Location	Description	$\delta^{18}\text{O}$ SMOW	$\delta^{18}\text{O}$ PDB	$\delta^{13}\text{C}$ PDB	Crystallization temperature	$\delta^{18}\text{O}$ fluid (‰)
Milky quartz	DTR306	Guaysimi Central	Milky quartz in gold-rich type I	12.6			400±50°C	7.3 to 9.5
	DTR341	Nambija-El Playon	Idem	12.6			400±50°C	7.3 to 9.5
	DTR505a	Guaysimi Banderas	Idem	14.6			400±50°C	9.3 to 11.5
	DTR505b		Idem	11.4			400±50°C	6.2 to 8.4
	DTR505b		Idem	11.7			400±50°C	6.4 to 8.6
	DTR339	Cambana	Milky quartz in vug	9.2			400±50°C	4.0 to 6.2
	DTR384	Campanillas	Idem	11.3			400±50°C	6.1 to 8.3
	DTR388		Milky quartz in type I vein	10.4			400±50°C	5.1 to 7.3
Quartz in sulfide-rich type III veins	DTR357	Nambija-El Tierrero	Type III vein in brown garnet skarn	11.1			300±50°C	2.2 to 5.8
	DTR358		Molybdenite-bearing type III vein	9.3			300±50°C	0.4 to 4.0
	DTR411	Guaysimi central	Type III vein in brown garnet skarn	11.1			300±50°C	2.2 to 5.8
	DTR411		Idem	11.5			300±50°C 2	6 to 6.2
	DTR509	Guaysimi Banderas	Type III vein in volcanoclastic rocks	10.7			300±50°C	1.8 to 5.4
Comb quartz	DTR37	Campanillas	Comb quartz and hematite in vug	6.2			175±25°C	-9.1 to -5.4
	DTR500b		Comb quartz in type I vein	5.3			175±25°C	-10.0 to -6.3
	DTR500b		Idem	5.3			175±25°C	-10.0 to -6.3
Mix of milky and comb quartz	DTR309a	Cambana	Milky and comb quartz in vug	9.3				
	DTR309a		Idem	9.1				
	DTR309a		Idem	8.6				
	DTR 311a		Idem	11.1				
	DTR 311a		Idem	7.9				
	DTR 311a		Idem	9.5				
	DTR362	Guaysimi Central	Milky and comb quartz in vug	8.7				
	DTR383	Campanillas	Idem	7.8				
	DTR500a		Milky and comb quartz in type I	8.1				
Calcite in vugs	DTR 309b	Cambana	Vug	6.8	-23.4	-10.0	175±25°C	-5.8 to -2.7
	DTR 309b		Idem	7.0	-23.2	-10.0	175±25°C	-5.7 to -2.6
	DTR 311b		Idem	6.8	-23.4	-8.6	175±25°C	-5.8 to -2.7
	DTR 311b		Idem	6.8	-23.4	-8.8	175±25°C	-5.9 to -2.8
	DTR 327	Campanillas	Idem	7.1	-23.1	-8.9	175±25°C	-5.6 to -2.5
	DTR 327		Idem	7.6	-22.6	-9.0	175±25°C	-5.1 to -2.0
	Calcite in late faults	DTR 410	Guaysimi central	Late fault	15.0	-15.4	-8.3	140±20°C
DTR 410		Idem		14.6	-15.8	-8.4	140±20°C	-0.5 to 2.7

Isotopic compositions for fluids are calculated at temperatures derived from the fluid inclusion study and the mineral assemblages, the quartz-H₂O fractionation curve from Matsuhisa et al. (1979), and the calcite-H₂O fractionation curve from O'Neil et al. (1969)

Table 4). Fluid inclusions of the L3 and L3h types observed in this comb quartz allowed us to estimate formation temperature in the range of 150°C to 200°C (Fig. 5b). For these temperatures, the equilibrium $\delta^{18}\text{O}_{\text{water}}$ values of comb

quartz precipitating fluids lie between -10.0‰ and -5.4‰ (Fig. 8a and Table 4).

Calcite in the same late assemblage filling cavities and veins has $\delta^{18}\text{O}$ values of 7.6‰ to 6.8‰ and $\delta^{13}\text{C}$ values of

–8.6‰ to –10‰ relative to VPDB (Fig. 8 and Table 4). Values of $\delta^{18}\text{O}_{\text{water}}$ between –5.9‰ and –2.0‰ (Fig. 8a and Table 4) have been obtained using the fractionation equation of O'Neil et al. (1969) and formation temperatures between 150°C and 200°C, estimated from L3 fluid inclusions in calcite in vugs and type I veins and which are similar to those obtained for the comb quartz (Fig. 5b).

Milky quartz samples containing significant amounts of late-stage clear comb quartz and/or calcite have $\delta^{18}\text{O}$ values between 11.1‰ and 7.8‰ (Table 4), i.e., lower than pure milky quartz (14.6–9.2‰). No temperature estimation has been done for these mixed samples.

Calcite in late faults

Calcite in late faults has higher $\delta^{18}\text{O}$ values (15‰ to 14.6‰) but similar $\delta^{13}\text{C}$ values (–8.3‰ to –8.4‰, Fig. 8b). Fluid inclusion analyses suggest that calcite in late faults was deposited between 120°C and 160°C and the calculated $\delta^{18}\text{O}_{\text{water}}$ values range from –0.5‰ to 3.1‰ (Fig. 8a and Table 4).

Discussion

The results of this study confirm that the Nambija skarns are coeval with potassic and potassic-sodic metasomatism affecting respectively the porphyritic intrusions and the volcanosedimentary rocks of the Piuntza unit.

The available data do not allow us to discuss the fluid evolution separately in the different Nambija deposits. However, crosscutting relationships and systematic geometric patterns of retrograde vugs and veins (Fig. 2) allow us to recognize similar fluid inclusion and stable isotope trends across different deposits. In addition, the fact that the precise zircon and titanite U–Pb and molybdenite Re–Os dating gives, within errors, the same magmatic crystallization and mineralization ages suggest that the genetic processes were comparable in large parts of the district. Taken together, the fluid inclusion and the stable isotope compositions record a plausible fluid evolution for the Nambija skarns.

Figure 8 shows a pressure–temperature diagram where the isochores of all Lc aqueous-carbonic fluid inclusions (hosted in magmatic quartz, B vein quartz, garnet of blue–green quartz, and milky quartz) and representative Lh halite-bearing fluid inclusions hosted in pyroxene have been plotted. These isochores allow us to define a high-pressure domain (around 120–100 MPa corresponding to around 4-km depth assuming lithostatic pressure) for the prograde stage ($T > 500^\circ\text{C}$) and a domain of lower pressure for $T > 450^\circ\text{C}$.

The high-pressure domain for most of the prograde stage is only loosely defined on the basis of the Lh halite-bearing

fluid inclusions hosted in pyroxene and the two Lc fluid inclusions in magmatic quartz and B vein with Th of 506°C and 565°C, respectively. The latter, as most of the Lc fluid inclusions and the Lh fluid inclusions in magmatic quartz (see above), are re-equilibrated possibly during isobaric cooling. However, Vityk and Bodnar (1995, 1998) show that, in case of isobaric cooling, the fluid inclusions having the highest Th are those that have been the least affected by re-equilibration and would yield the best approximation of the actual PT trapping conditions (Fig. 2b in Vityk and Bodnar 1995). At Nambija, this assumption is supported by the broad PT field occupied by Lc fluid inclusions in magmatic quartz, showing re-equilibration features (broken lines in Fig. 8). Therefore, we have assumed that the isochores of the two Lc fluid inclusions in magmatic quartz and B vein with Th of 506°C and 565°C represent a good approximation of real conditions. With this assumption, it can be estimated from Lc fluid inclusions with the highest Th (i.e., above 500°C) that pressure during most of the prograde stage was probably around 100–120 MPa (pressure estimated using equation states of Duan et al. 1995 and Bakker 1999) corresponding to about 4-km depth assuming lithostatic conditions (Fig. 8).

The domain with lower pressures, between 100 and 50 MPa, is defined by flat isochores of most Lc fluid inclusions which do not show re-equilibration features and that homogenize between 450°C and 350°C. Even with a temperature correction of 100°C, the pressures would remain between 100 and 50 MPa, i.e., lower than the minimum pressures indicated by the high-temperature Lc fluid inclusions.

It can be inferred that the high-temperature (500°C to $>600^\circ\text{C}$), high-salinity (up to 65 wt.% eq. NaCl) and moderate- to low-salinity fluids (1.0 to 23 wt.% eq. NaCl) recorded in Lh and H_2O – CO_2 –NaCl Lc fluid inclusions of prograde minerals were derived from boiling of a magmatic aqueous-carbonic (5–10 mol% CO_2) fluid of moderate salinity (6–12 wt.% eq. NaCl, Fig. 9, arrow 1 in Fig. 10). Such a fluid would be similar to those recognized in other intrusion-related deposits (e.g., McCoy et al. 1997; Baker 2002). During its ascent, this moderate saline fluid would intersect its solvus at approximately 200 MPa at 600°C and separate into a high-salinity CO_2 -poor liquid phase and a moderately saline CO_2 -rich vapor phase (e.g., Frantz et al. 1992; Duan et al. 1995; Fig. 9a, b).

As summarized by Kwak (1986) and Gilg (1996), the presence of aqueous-carbonic fluids in an anhydrous prograde skarn assemblage is unusual. Therefore, it could be argued that the high-temperature low-salinity H_2O – CO_2 –NaCl Lc fluid inclusions are secondary and unrelated to the skarn formation. However, the CO_2 concentrations of these Lc fluid inclusions are possibly lower than 1 mol% (Table 2) and such low CO_2 concentrations have already

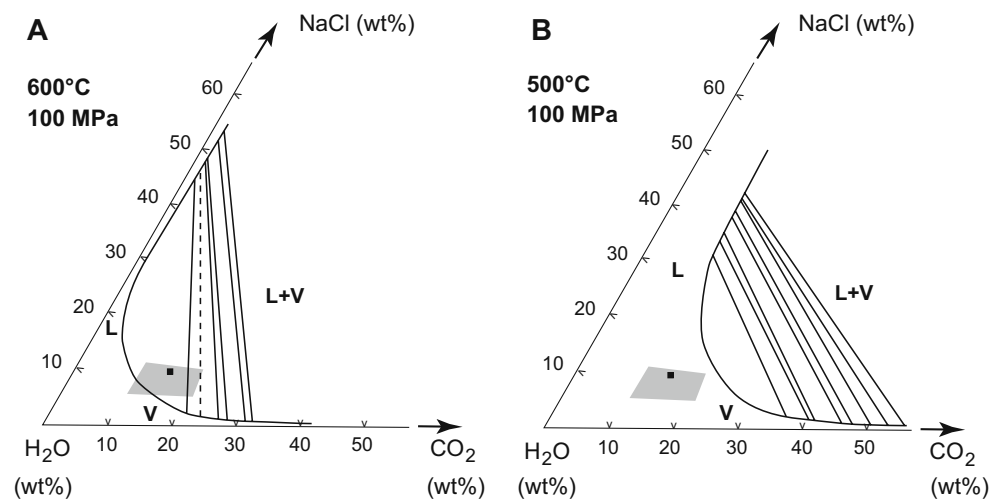


Fig. 9 Triangular plots showing the immiscibility boundaries and tie lines in the NaCl–H₂O–CO₂ system as a function of temperature and pressure (modified from Frantz et al. 1992; Duan et al. 1995). The diagram's units are in weight percent. The *black square* represents the 7.3 mol% CO₂–11.6 wt.% eq. NaCl relative to H₂O (15 wt.% CO₂–9.9 wt.% eq. NaCl) fluid trapped at a pressure around 140 MPa in coarse-grained B vein quartz in the altered Fortuna porphyritic intrusion. The *gray field* represents the estimated composition of the single-phase magmatic aqueous-carbonic fluid (5–10 mol% CO₂ and

6–12 wt.% eq. NaCl relative to H₂O, i.e., 10.6–20.7 wt.% CO₂ and 5.3–10.8 wt.% eq. NaCl), from which the high-salinity fluids and moderate- to low-salinity aqueous-carbonic fluids found in high-temperature Lh and Lc fluid inclusions can be derived. Diagrams A and B show that this single-phase fluid will undergo phase separation at 600°C below 200 MPa and diagrams C and D show that cooling to 500°C (temperature recorded in some Lc, L1, and L2 fluid inclusions) at constant pressure would inhibit phase separation

been reported in fluid inclusions in skarn garnets (Kwak and Tan 1981; Gilg 1996). In addition, modeling of phase equilibria shows that garnet can be formed from fluid containing up to 1 mol% CO₂ (Einaudi et al. 1981; Gilg 1996; Meinert et al. 2005).

All inclusions (Lc, L1, and L2, Fig. 10a) in blue–green garnet skarn and late honey-yellow garnet in clusters and veins (interpreted to represent the transition to the retrograde stage) contain fluids with salinities below 20 wt.% eq. NaCl and homogenization temperatures between 513°C and 294°C. This group of fluid inclusions as well as those in milky quartz of vugs and type I veins and in fractures in magmatic quartz show a rough tendency to lower salinities with decreasing homogenization temperatures. This temperature interval is interpreted to reflect the transition between the last prograde fluids (precipitating honey-yellow garnet) and retrograde fluids (precipitating milky quartz in vugs and type I veins, Figs. 8 and 10a).

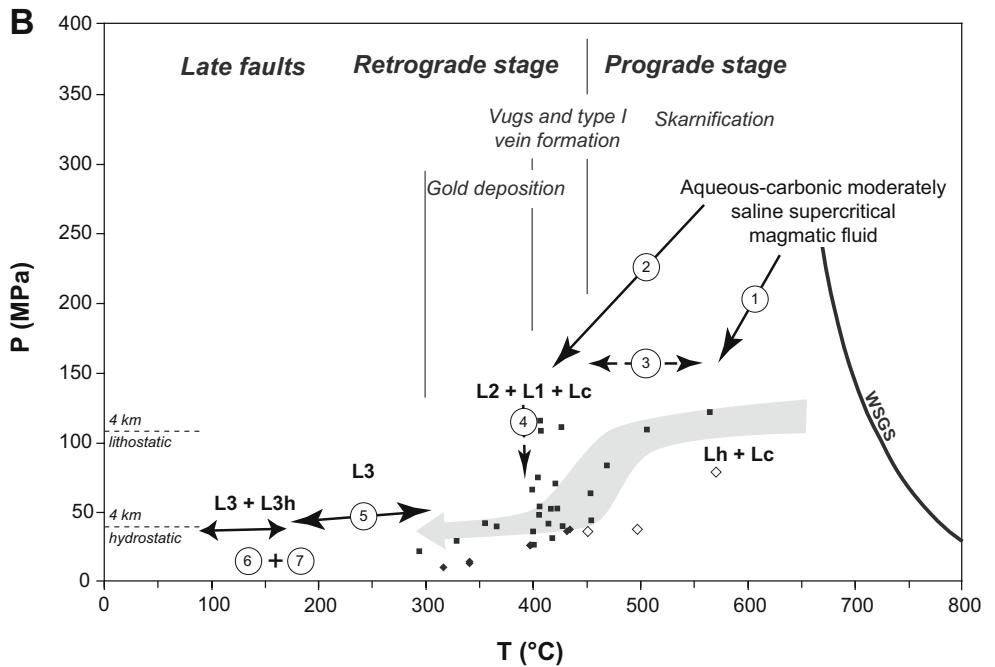
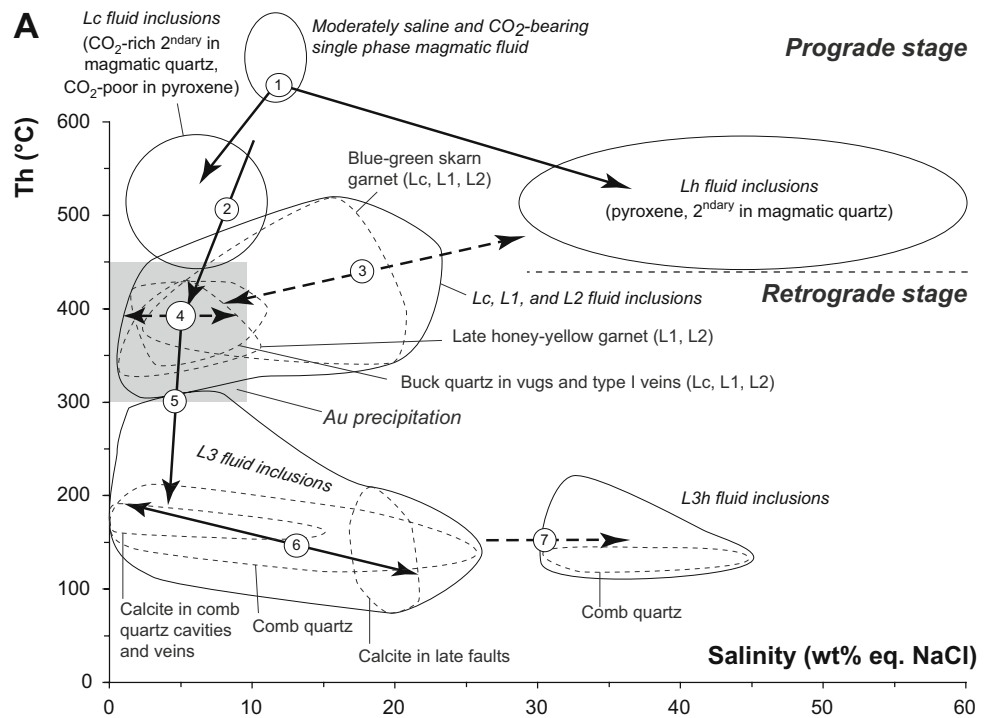
The progressive decrease in salinity with decreasing homogenization temperature (down to 294°C, Fig. 10a) may be due, at least in part, to the presence of supercritical magmatic aqueous-carbonic fluids of moderate salinity which have not abandoned the single-phase liquid field and that underwent mixing with low-salinity fluids. This evolution could happen during cooling at relatively constant pressure (Fig. 9a, b) as suggested by Meinert et al. (1997, 2003) for other skarn deposits. Typical magmatic $\delta^{18}\text{O}$ values (6.2‰ to 11.5‰) of fluids depositing milky quartz in gold-rich vugs and type I veins are consistent with

the hypothesis that at the prograde–retrograde stage transition, the skarn fluids were dominated by fluids of magmatic origin.

The presence of very-low-salinity fluid inclusions with homogenization temperatures in the range of 300°C to 400°C could be explained by boiling (Fig. 8, arrow 4 in Fig. 10) due to the pressure decrease recognized between the prograde and the retrograde stages. The dilational character of type I veins (Fontboté et al. 2004) would also be consistent with such a pressure decrease. The oxidized character of the magmatic fluid responsible for the garnet dominant prograde assemblage in the exoskarn (Fontboté et al. 2004; Markowski et al. 2006) is in accordance with the porphyry environment in a continental arc setting, as proposed for the coeval Pangui porphyry copper belt (Prodeminca 2000; Gendall et al. 2000; Chiaradia et al. 2009). The high hematite-to-pyrite ratio in gold-bearing assemblages (Fontboté et al. 2004; Markowski et al. 2006) is probably the consequence of the low fluid-to-rock ratio during the retrograde stage and of the oxidizing character of the prograde mineralogy, dominated by Fe³⁺-bearing garnet.

The fact that chlorite composition reflects the composition of their host skarn type (Mg rich in the pyroxene-epidote skarn and Fe and Al rich in the brown and blue–green skarns) also points to low fluid-to-rock ratios, which would explain the small extent of the retrograde alteration. $\delta^{18}\text{O}$ values of fluids forming quartz, chlorite, sericite, epidote, and calcite (below 350°C) in type III veins

Fig. 10 Model of fluid evolution in the Nambija skarns. The inferred moderately saline and CO₂-bearing single-phase magmatic fluid (1) underwent phase separation at a minimum temperature of 600°C and pressure around 150 MPa and evolves to high-salinity fluids and to moderate- to low-salinity aqueous-carbonic fluids responsible for the prograde stage. After cooling below 500°C at pressure still around 100–120 MPa, new pulses of the single-phase magmatic fluid (2) did not undergo phase separation and partly mixed (3) with residual hypersaline fluids before precipitating milky quartz in vugs and type I veins between 450°C and 350°C. A pressure decrease that probably induced local boiling is recorded at around 400°C (4). Gold deposition occurred below 350°C by cooling. Magmatic fluids mixed with meteoric fluids during type III vein formation (5). Meteoric fluids are dominant during comb quartz and calcite deposition in cavities and veins below 200°C. Basinal brines invaded the system, mixed (6) with meteoric fluids and deposited calcite in late faults. High salinities of the low-temperature L3h fluid inclusions are the result of post-trapping modification (7) affecting L3 fluid inclusions



Process	Mainly recorded in
1: boiling (inferred)	Pyroxene, secondary fluid inclusions in magmatic quartz
2: cooling of the single phase magmatic fluid	Blue-green skarn and late honey-yellow garnet and buck quartz
3: mixing with residual hypersaline fluids	Blue-green skarn garnet
4: pressure drop and local boiling	Late honey-yellow garnet and buck quartz
5: mixing between magmatic and meteoric fluid + cooling	comb quartz, calcite and secondary fluid inclusions in buck quartz in vugs and type I veins
6: mixing between meteoric fluid and basinal brines	Comb quartz and calcite in vugs and type I veins
7: post-trapping salinity increase (L3 -> L3h)	Comb quartz

(no fluid inclusions available) ranging from 0.4‰ to 6.2‰ (Fig. 7a and Table 4) suggest mixing between late pulses of magmatic fluids and meteoric fluids invading the system (arrow 5 in Fig. 10).

The transition from Lc to CO₂-free L1/L2 fluid inclusions during cooling is consistent with the fact that at low temperature calcite precipitates instead of milky quartz. This evolution may be due to CO₂ effervescence (Drummond and Ohmoto 1985; Fournier 1985a; Fournier 1985b) because of pressure decrease. The pH increase that results from CO₂ effervescence together with decreasing temperature are two powerful mechanisms to destabilize gold-transporting chloride complexes below 400°C (Gammons and Williams-Jones 1997) and explain the common association of native gold grains and calcite. The hypothesis of gold transport by chloride complexes is favored because of the high hematite-to-pyrite ratio of gold-bearing samples and the general low sulfide content in all the deposits of the Nambija district.

Post-ore veins

Low-temperature (<300°C) fluids responsible for the precipitation of comb quartz and calcite in cavities and veins are recorded in aqueous L3 fluid inclusions. Their tendency of having higher salinities with decreasing homogenization temperatures (Figs. 5, 10) can be explained in terms of mixing (arrow 6 in Fig. 10) with low-temperature moderately saline fluids (in the range of about 100°C and 25 wt.% eq. NaCl).

The high-salinity values measured in L3h fluid inclusions, which homogenize by halite melting (Fig. 5a and Table 1), are interpreted as the result of post-trapping modification (arrow 7 in Fig. 10) according to the mechanism proposed by Audetat and Günther (1999). An alternative explanation by a boiling process would imply unrealistically low pressures (<1.5 MPa, i.e., <150-m depth under hydrostatic conditions, following data of LV curves of Khaibullin and Borisov 1966) for temperatures below 200°C.

Ingression of meteoric fluids is recorded by O isotope compositions of comb quartz ($\delta^{18}\text{O}_{\text{water}}$ between -10.0‰ and -5.4‰) and associated calcite ($\delta^{18}\text{O}_{\text{water}}$ between -5.9‰ and -2.0‰) in cavities and veins (Fig. 7a and Table 4). Discrepancies between $\delta^{18}\text{O}_{\text{water}}$ calculated from comb quartz and associated calcite could be the result of isotopic re-equilibration of calcite associated with comb quartz during deposition of calcite in late faults from fluids with higher $\delta^{18}\text{O}_{\text{water}}$ values (see below). Sample DTR327 for example shows locally late calcite veins crosscutting comb quartz and associated calcite.

Carbon isotope compositions of calcite associated with comb quartz are those typical for magmatic calcites (Fig. 7a and Table 4), although a fluid equilibrated with magmatic rocks cannot be excluded simply on the basis of the $\delta^{13}\text{C}$

values. Carbon isotope analysis of the calcite in late faults gives similar results (Fig. 7a and Table 4). The low-temperature moderate- to high-salinity fluids trapped as L3 fluid inclusions in calcite in late faults have similar microthermometric characteristics as the low-temperature moderate-salinity fluids involved in the mixing process proposed above to explain the salinity range of fluid inclusions in comb quartz and calcite in cavities and veins (Fig. 5b). Taking into account their $\delta^{18}\text{O}$ values (-0.5‰ to 3.1‰) and their salinities, these fluids can be interpreted to be basinal brines (Fig. 7 and Table 4). Ingression of basinal brines is probably related to the formation of the Early Cretaceous basin hosting the marine Hollín Formation prior to uplifting of the sub-Andean zone during Late Cretaceous to Paleocene (Spikings et al. 2000; Hughes and Pilatasig 2002; Jaillard et al. 2005; Pratt et al. 2005).

Comparison with other gold skarn system

At the oxidized gold skarn of McCoy (Brooks et al. 1991; Brooks, 1994), the obtained isochores, the absence of CO₂-bearing fluids, and the occurrence of breccias indicate a shallower level of formation (depth of about 2 km) compared to the Nambija district (depths of about 4 km). The temperatures and salinities of fluid from the prograde and retrograde stage at Big Gossan (Meinert et al. 1997) have a similar evolution as at Nambija. However, at Big Gossan, mineralization, mainly occurring in the matrix of a breccia, is of the copper-gold type and skarns were also formed at shallower levels (around 2 km). Moreover, no CO₂-bearing fluid inclusions were reported at Big Gossan. In contrast, the Nambija deposits are devoid of breccias and have veins (type I, II) comparable to those formed in the early evolution stages of porphyry systems (Fontboté et al. 2004; Chiaradia et al. 2009), all features being consistent with the depths of about 4 km derived from the fluid inclusion results.

Carbon-dioxide-bearing fluids in gold skarn systems were observed in the reduced gold skarn deposits of the Rio Narcea Gold belt in Spain (Arcos et al. 1995; Arcos 1996; Martin-Izard et al. 2000). In these deposits, carbon-dioxide-bearing fluids were observed in gold-bearing quartz that post-dates prograde calc-silicates and are interpreted to be the low-density phases coexisting with an immiscible high-density and high-salinity phase. Fluid evolution in the Rio Narcea gold skarn shows similarities with that of Nambija. A main difference compared to Nambija is the presence of fluids with higher amounts of CO₂ at temperatures below 400°C. This could be explained by a deeper level of skarn formation (5–6 km after Arcos et al. 1995 and Arcos 1996) because increasing pressure favors higher CO₂ solubility in H₂O–NaCl fluids (e.g., Gehrigh 1980; Baker 2002).

Conclusions

The fluid inclusion and stable isotope results of prograde minerals from the oxidized Nambija skarns indicate the coexistence at high temperatures (500°C to >600°C) of high-salinity (up to 65 wt.% eq. NaCl) and moderate- to low-salinity aqueous fluids with traces of CO₂. They are interpreted to have been trapped at pressures around 100–120 MPa, i.e., 4-km depth for the main part of the prograde skarn stage. This depth is consistent with the finding that skarn formation is coeval and transitional with K and Na metasomatism affecting both the porphyritic intrusions and the host rocks of the Piuntza unit. High-temperature and high-salinity fluids characterize the porphyritic intrusions spatially associated with skarn bodies at Fortuna and Campanillas. Higher CO₂ contents in the moderate- to low-salinity fluids of the porphyritic intrusions are attributed to higher temperature conditions compared to the exoskarn.

The data also offer an explanation for one of the most striking features of the Nambija skarns, which is the weak development of retrograde alteration despite high gold grades being deposited during the retrograde stage. Our results, in accordance with the hypothesis proposed for other Au-bearing skarns by Meinert et al. (2003), suggest that not only the prograde stage but also the main part of the retrograde alteration is dominated by magmatic fluids. The results are also consistent with retrograde low- to moderate-saline fluids recorded at Nambija being supercritical magmatic aqueous-carbonic fluids that have cooled without abandoning the single-phase field and have partly undergone mixing with condensed magmatic vapors.

Ingression of meteoric fluids and/or basinal brines is limited to the late evolutionary stages, at temperatures below 300°C. The relatively warm (Th=350–450°C) moderate- to low-salinity fluids from which milky quartz infilling vugs and type I veins precipitated appear to be dominantly magmatic. Fluids in equilibrium with the gold-bearing milky quartz have δ¹⁸O values compatible with a magmatic origin. Paragenetic observations indicate that gold was precipitated with calcite, chlorite, and hematite at the end of this stage, possibly below 350°C, as a result of pH increase, related to CO₂ effervescence and/or cooling, both resulting in the destabilization of gold-bearing chloride complexes (Gammons and Williams-Jones 1997). Ingression of external fluids is only recorded for post-ore stages.

The depth of the skarn system (approximately 4 km) may account for why magmatic fluids are dominant up to relatively low temperatures since the amounts of external fluids that could enter the system at this depth is expected to be limited. As a result, the total amount of fluid present during most of the retrograde stage was low and dominantly magmatic, explaining the small amount of retrograde alteration. The compositional variability of chlorite is also

indicative of low water-to-rock ratios as the cation content reflects the composition of the replaced prograde minerals. Despite the low water-to-rock ratio, the oxidizing magmatic fluid was not reduced by fluid–rock interaction because of the oxidized character of the prograde skarn mineralogy, dominated by Fe³⁺-bearing garnet.

Nambija would represent a rather deep equivalent of the oxidized gold skarn class (e.g., McCoy and Wabu) interpreted to have formed at 2-km depth (Brooks et al. 1991; Brooks 1994; Allen and Aslund 1998). This greater depth of formation could explain the presence in the Nambija skarns of moderate amounts of aqueous-carbonic fluids.

Acknowledgement The research presented herein was supported by the Swiss National Science Foundation, as project 2000-062 000.00. We thank Comcumay S.A. (Campanillas mine), Cominza S.A. (Guaysimi mines), Compañía Minera del Ecuador-Andos (Nambija-Mapasingue mine), Compañía Minera Sol de Oriente (Cambana mine), Cooperativa Once de Julio (Nambija condominios), and Fortuna Gold Mining Corporation (Fortuna mine) for access to their mines and properties and for helpful assistance in the field. This paper benefited from discussions with A. de Haller, C. Heinrich, and L. Meinert. We thank A Gilg, D Lentz, and A Mueller for their careful reviews that helped to improve this manuscript.

References

- Allen J, Aslund T (1998) The Wabu gold skarn, Irian Jaya, Indonesia. *The Gangee, Newsletter of the Mineral Deposit Division. Geol Assoc Canada* 59:9–11
- Arcos D, Soler A, Delgado J (1995) Fluid evolution in the Cu–Au deposit related to the Carlés Granodiorite (Asturias). *Eur J Mineral* 8:975–985
- Arcos D (1996) Las mineralizaciones asociadas a la granodiorita en el deposito de Cu-Au de Carlés (Asturias). Unpublished Ph.D. thesis, Barcelona University, Spain, 294 pp
- Audetat A, Günther D (1999) Mobility and H₂O loss from fluid inclusions in natural quartz crystals. *Contrib Mineral Petrol* 137:1–14
- Baker T (2002) Emplacement depth and carbon dioxide-rich fluid inclusions in intrusion-related gold deposits. *Econ Geol* 97:1111–1117
- Bakker RJ (1999) Adaptation of the Bowers and Helgeson (1983) equation of state to the H₂O–CO₂–CH₄–N₂–NaCl system. *Chem Geol* 154:225–236
- Bakker RJ, Brown PE (2003) Computer modeling in fluid inclusion research. In: Samson I, Anderson A, Marshall D (eds) *Fluid inclusion analysis and interpretation. Mineralogical Association of Canada short course series, vol 32. Mineralogical Association of Canada, Quebec*, pp 175–212
- Bodnar RJ, Burnham CW, Sterner SM (1985) Synthetic fluid inclusions in natural quartz: III. Determination of phase equilibrium properties in the system H₂O–NaCl to 1000°C and 1500 bars. *Geochim Cosmochim Acta* 49:1861–1873
- Bodnar RJ (1994) Synthetic fluid inclusions. XII. Experimental determination of the liquidus and isochores for a 40 wt.% H₂O–NaCl solution. *Geochim Cosmochim Acta* 58:1053–1063
- Bodnar RJ, Vityk MO (1994) Interpretation of microthermometric data for H₂O–NaCl fluid inclusions. In: De Vivo B, Frezzotti ML

- (eds) Fluid inclusions in minerals. Methods and applications. Virginia Tech, Blacksburg, pp 117–130
- Brooks JW, Meinert LD, Kuyper BA, Lane ML (1991) Petrology and geochemistry of the McCoy gold skarn, Lander County, NV. In: Raines GL, Lisle RE, Schafer RW, Wilkinson WH (eds) Geology and ore deposits of the Great Basin. Geol Soc Nevada, Reno, pp 419–442
- Brooks JW (1994) Petrology and geochemistry of the McCoy gold skarn, Lander County, Nevada. Unpublished Ph.D. thesis, Washington State University, Pullman, Washington, 607 pp
- Bowman JR (1998) Stable-isotope systematics of skarns. In: Lentz DR (ed) Mineralized intrusion related skarn systems. Mineralogical Association of Canada short course series, vol 26. Mineralogical Association of Canada, Quebec, pp 99–145
- Burke EAJ (2001) Raman microspectrometry of fluid inclusions. *Lithos* 55:139–158
- Cathelineau M (1988) Cation site occupancy in chlorites and illites as a function of temperature. *Clay Miner* 23:471–485
- Chiaradia M, Vallance J, Fontboté L, Stein HJ, Schaltegger U, Coder J, Richards J, Villeneuve M, Gendall I (2009) U–Pb, Re–Os, and $^{40}\text{Ar}/^{39}\text{Ar}$ geochronology of the Nambija Au-skarn and Pangui porphyry Cu deposits, Ecuador: implications for the Jurassic metallogenic belt of the Northern Andes. *Miner Deposita*. doi:10.1007/s00126-008-0210-6
- Diamond LW (2003) Introduction to gas-bearing aqueous fluid inclusions. In: Samson I, Anderson A, Marshall D (eds) Fluid inclusions: analysis and interpretation. Mineralogical Association of Canada short course series, vol 32. Mineralogical Association of Canada, Quebec, pp 101–159
- Drummond SE, Ohmoto H (1985) Chemical evolution and mineral deposition in boiling hydrothermal systems. *Econ Geol* 80:126–147
- Duan Z, Møller N, Weare JH (1995) Equation of state for the $\text{NaCl-H}_2\text{O-CO}_2$ system: prediction of phase equilibria and volumetric properties. *Geochim Cosmochim Acta* 59:2869–2882
- Dubessy J, Poty B, Ramboz C (1989) Advances in C–O–H–N–S: fluid geochemistry based on micro Raman spectrometric analysis of fluid inclusions. *Eur J Mineral* 1:517–534
- Einaudi MT, Meinert LD, Newberry RJ (1981) Skarn deposits. *Econ Geol* 75:317–391
- Fontboté L, Vallance J, Markowski A, Chiaradia M (2004) Oxidized gold skarns in the Nambija district, Ecuador. In: Perrello J, Sillitoe R, Vidal C (eds) Andean metallogenesis: new discoveries, concepts, and updates. Society of Economic Geologists Special Publication 11. Society of Economic Geologists, Littleton, pp 341–357
- Foster MD (1962) Interpretation of the composition and a classification of the chlorites. *US Geol Prof Paper* 414A:33p
- Fournier RO (1985a) The behavior of silica in hydrothermal solutions. In: Berger BR, Bethke PM (eds) Geology and geochemistry of epithermal systems. Reviews in economic geology, vol 2. Society of Economic Geologists, Littleton, pp 45–62
- Fournier RO (1985b) Carbonate transport and deposition in the epithermal environment. In: Berger BR, Bethke PM (eds) Geology and geochemistry of epithermal systems. Reviews in economic geology, vol 2. Society of Economic Geologists, Littleton, pp 63–72
- Frantz JD, Popp RK, Hoering TC (1992) The compositional limits of fluid immiscibility in the system $\text{H}_2\text{O-NaCl-CO}_2$ as determined with the use of synthetic fluid inclusions in conjunction with mass spectrometry. *Chem Geol* 98:237–255
- Gammons CH, Williams-Jones AE (1997) Chemical mobility of gold in the porphyry-epithermal environment. *Econ Geol* 92:45–59
- Gehrig M (1980) Phasengleichgewichte und pVT-Daten ternärer Mischungen aus Wasser, Kohlendioxid und Natriumchlorid bis 3 kbar und 550°C. Ph.D. thesis, Univ. Karlsruhe, in German
- Gendall IR, Quevedo LA, Sillitoe RH, Spencer RM, Puente CO, Leon JP, Povedo RR (2000) Discovery of a Jurassic porphyry copper belt, Pangui area, southern Ecuador. *SEG Newslett* 43(1):8–15
- Gilg HA (1996) Fluid inclusion and isotope constraints on the genesis of high-temperature carbonate-hosted Pb–Zn–Ag deposits. In: Sangster D (ed) Carbonate-hosted lead zinc deposits SEG special publication 4. SEG, Littleton, pp 501–514
- Goldstein RH, Reynolds TJ (1994) Systematics of fluid inclusions in diagenetic minerals. SEPM short course no. 31. SEPM, Tulsa, p 199
- Gustafson LB, Hunt JP (1975) The porphyry copper deposit at El Salvador. *Chile Econ Geol* 70:856–912
- Hammarstrom JM (1992) Mineralogy and chemistry of gold-associated skarn from Nambija, Zamora Province, Ecuador: a reconnaissance study: advances related to US and international mineral resources. USGS, Reston, pp 107–118
- Hughes RA, Pilatasig LF (2002) Cretaceous and Tertiary terrane accretion in the Cordillera Occidental of the Andes of Ecuador. *Tectonophysics* 345:29–48
- Jaillard E, Guillier B, Bonnardot MA, Hassani R, Lapierre H, Toro J (2005) Orogenic buildup of the Ecuadorian Andes. In: Sempéré T (ed) 6th International Symposium on Andean Geodynamics (ISAG 2005, Barcelona), extended abstracts, pp 404–407
- Jowett EC (1991) Fitting iron and magnesium into the hydrothermal chlorite geothermometer. In: GAC/MAC/SEG Joint Annual Meeting (Toronto), Program with Abstracts 16, p 62
- Kasemann S, Meixner A, Rocholl A, Vennemann T, Schmitt A, Wiedenbeck M (2001) Boron and oxygen isotope composition of certified reference materials NIST SRM 610/612, and reference materials JB-2G and JR-2G. *Geostand Newslett* 25:405–416
- Khaibullin IK, Borisov NM (1966) Experimental investigation of the thermal properties of aqueous and vapour solutions of sodium and potassium chlorides at phase equilibrium (in Russian). *Teplofizika Vysokikh Temperatur* 4:518–523
- Knight CL, Bodnar RJ (1989) Synthetic fluid inclusions: IX. Critical PVTX properties of $\text{NaCl-H}_2\text{O}$ solutions. *Geochim Cosmochim Acta* 53:3–8
- Kwak TAP, Tan TH (1981) The geochemistry of Zoning in skarn minerals at the King Island (Dolphin) Mine. *Econ Geol* 76:468–497
- Kwak TAP (1986) Fluid inclusions in skarns (carbonate replacement deposits). *J Metam Geol* 4:363–384
- Litherland M, Aspden JA, Jemielita RA (1994) The metamorphic belts of Ecuador. Overseas memoir 11. BGS, Keyworth, p 147
- Markowski A, Vallance J, Chiaradia M, Fontboté L (2006) Mineral Zoning and Gold occurrence in the Fortuna skarn Mine, Nambija district, Ecuador. *Miner Deposita* 41:301–321
- Martin-Izard A, Paniagua A, García-Iglesias J, Fuertes-Fuente M, Ll B, Maldonado C, Varela A (2000) The Carlés copper–gold–molybdenum skarn (Asturias, Spain): geometry, mineral associations and metasomatic evolution. *J Geoch Expl* 71:153–175
- Matsuhisa Y, Goldsmith JR, Clayton RN (1979) Oxygen isotopic fractionation in the system quartz–albite–anorthite–water. *Geochim Cosmochim Acta* 43:1131–1140
- McCoy D, Newberry RJ, Layer PW, Di Marchi JJ, Bakke AA, Masterman JS, Minehane DL (1997) Plutonic-related gold deposits of interior Alaska. In: Goldfarb RJ, Miller LD (eds) Ore deposits of Alaska Economic geology monograph 9. SEG, Littleton, pp 191–241
- Meinert LD, Hefton KK, Mayes D, Tasiran I (1997) Geology, zonation, and fluid evolution of the Big Gossan Cu–Au skarn deposit, Ertzberg district, Irian Jaya. *Econ Geol* 92:509–533
- Meinert LD (2000) Gold in skarns related to epizonal intrusions. In: Hagemann SG, Brown PE (eds) Gold in 2000. Reviews in Economic Geology, vol 13. SEG, Littleton, pp 347–375

- Meinert LD, Hedenquist JW, Satoh H, Matsuhisa Y (2003) Formation of anhydrous and hydrous skarn in Cu–Au ore deposits by magmatic fluids. *Econ Geol* 98:147–156
- Meinert LD, Dipple GM, Nicolescu S (2005) World skarn deposits. In: Hedenquist JW, Thompson JFH, Goldfarb RJ, Richards JP (eds) *Econ Geol 100th Anniv*:299–336
- Oakes CS, Bodnar RJ, Simonson JM (1990) The system NaCl–CaCl₂–H₂O. I. The vapor-saturated ice liquidus. *Geochim Cosmochim Acta* 54:603–610
- O'Neil JR, Clayton RN, Mayeda TK (1969) Oxygen isotope fractionation in divalent metal carbonates. *J Chem Phys* 51:5547–5558
- Pratt WT, Duque P, Miguel P (2005) An autochthonous geological model for the eastern Andes of Ecuador. *Tectonophysics* 399:251–278
- Prodeminca (2000) Depositos porfídicos y epi-mesotermales relacionados con intrusiones de la Cordillera del Cóndor: Evaluación de distritos mineros del Ecuador: UCP Prodeminca Proyecto MEM BIRF 36-55 EC 5, 223 pp
- Rumble DIII, Hoering TC (1994) Analysis of oxygen and sulfur isotope ratios in oxide and sulfide minerals by spot heating with a carbon dioxide laser in a fluorine atmosphere. *Accounts Chem Res* 27:237–241
- Sharp ZD (1990) A laser-based microanalytical method for the in-situ determination of oxygen isotope ratios of silicates and oxides. *Geochim Cosmochim Acta* 54:1353–1357
- Shepherd TJ (1981) Temperature programmable heating-freezing stage for microthermometric analysis of fluid inclusions. *Econ Geol* 76:1244–1247
- Sheppard SMF (1986) Characterization and isotopic variations in natural waters. In: Valley JW, Taylor HP, O'Neil JR (eds) *Stable isotopes in high temperature geological processes Reviews in mineralogy*, vol 16. Mineralogical Society of America, Chantilly, pp 165–183
- Spikings RA, Seward D, Winkler W, Ruiz GM (2000) Low temperature thermochronology of the northern Cordillera Real, Ecuador: tectonic insights from zircon and apatite fission track analysis. *Tectonics* 19:649–668
- Spoetl C, Vennemann TW (2003) Continuous-flow IRMS analysis of carbonate minerals. *Rapid Comm Mass Spec* 17:1004–1006
- Sterner SM, Bodnar RJ (1984) Synthetic fluid inclusions in natural quartz. I. Compositional types synthesized and applications to experimental geochemistry. *Geochim Cosmochim Acta* 48:2659–2668
- Sterner SM, Hall DL, Bodnar RJ (1988) Synthetic fluid inclusions. V. Solubility relations in the system NaCl–KCl–H₂O under vapor-saturated conditions. *Geochim Cosmochim Acta* 52:989–1006
- Takenouchi S, Kennedy GC (1964) The binary system H₂O–CO₂ at high temperatures and pressures. *Am J Sci* 262:1055–1074
- Vallance J, Markowski A, Fontboté L, Chiaradia M (2003) Mineralogical and fluid inclusion constraints on the genesis of gold-skarn deposits in the Nambija district (Ecuador). In: Eliopoulos D et al. (eds). *Mineral exploration and sustainable development*, Millipress, vol. 1, pp 399–402
- Valley JW, Kitchen N, Kohn MJ, Niendorf CR, Spicuzza MJ (1995) UWG-2, a garnet standard for oxygen isotope ratios: strategies for high precision and accuracy with laser heating. *Geochim Cosmochim Acta* 59:5223–5231
- Velde B (1985) *Clay minerals a physico-chemical explanation of their occurrence*. Elsevier, Amsterdam, p 426
- Vityk MO, Bodnar RJ (1995) Textural evolution of synthetic fluid inclusions in quartz during re-equilibration, with applications to tectonic reconstruction. *Cont Miner Pet* 121:309–323
- Vityk MO, Bodnar RJ (1998) Statistical microthermometry of synthetic fluid inclusions in quartz during decompression. *Cont Miner Pet* 132:149–162